Vertical Hydrodynamic Focusing in an Isotropically Etched Glass Microfluidic Device

by

Tony An-tong Lin

B.S. Mechanical Engineering (2004)
The University of Texas at Austin

Submitted to the Department of Mechanical Engineering
in partial fulfillment of the requirements for the degree of

Master of Science in Mechanical Engineering

at the

MASSACHUSETTS INSTITUTE OF TECHNOLOGY

June 2007

© Massachusetts Institute of Technology 2007. All rights reserved.

Author .....
Department of Mechanical Engineering
May 21, 2007

Certified by .....
Daniel J. Ehrlich
Director, BioMEMS Lab
Whitehead Institute for Biomedical Research
Thesis Supervisor

Certified by .....
Anette Hosoi
Associate Professor of Mechanical Engineering
Thesis Supervisor

Accepted by .....
Lallit Anand
Professor of Mechanical Engineering
Chairman, Committee on Graduate Students

MASSACHUSETTS INSTITUTE OF TECHNOLOGY
JUL 18 2007
LIBRARIES
ARCHIVES

Vertical Hydrodynamic Focusing in an Isotropically Etched Glass Microfluidic Device

by

Tony An-tong Lin

Submitted to the Department of Mechanical Engineering
on May 21, 2007, in partial fulfillment of the
requirements for the degree of
Master of Science in Mechanical Engineering

Abstract

The development of microfluidic devices has enabled precision control of nanoliter-scale environments and reactions. Vertical hydrodynamic focusing is one possible way to improve the optical performance of these devices while maintaining precision control. Vertical hydrodynamic focusing was studied through the use of computation fluid dynamics (ADINA[1]) and experimental testing. It was found that the nonlinear effects of flow rate and geometry on the layering profile could be used to tune and correct the flow. A syringe pump-driven microfluidic device was fabricated out of isotropically etched and bonded glass plates and fluorescent confocal microscopy was used to verify computational models.

Thesis Supervisor: Daniel J. Ehrlich
Title: Director, BioMEMS Lab
Whitehead Institute for Biomedical Research

Thesis Supervisor: Anette Hosoi
Title: Associate Professor of Mechanical Engineering

[1] ADINA (Automatic Dynamic Incremental Nonlinear Analysis), ADINA R & D, Inc., Watertown, MA.

Acknowledgments

Working in the BioMEMS Lab has been a very challenging and fulfilling experience. I would like to thank Dr. Ehrlich for his mentorship and his guidance as I found my way through the research, often with one foot in engineering and the other in the new world of biology. I would like to thank Professor Hosoi for her always upbeat conversations and insight into my work. I would like to thank Professor Bathe and his group for helping me get set up with ADINA. Thank you to DuPont for a very generous fellowship and an awesome ride on the jet. Thank you to NIH for their support of the research. I would also like to thank my labmates. Thank you for welcoming me into the lab and taking the time to teach me all the things I didn't know. You kept me going and kept me company through many cold and wet days.

My experience at the Institute has been truly unique and one that I will always look back on with a smile. I would like to thank my parents and my brother for helping me get here (and get out). You have always pointed me in the right direction but allowed me to choose my own path, giving me unconditional love and support all along the way. To my friends: We have gotten to know each other through outrageous lunch time conversations, Wed night dinners, study sessions, all nighters, IM sports, coffee and beer. You have balanced and completed my experience here in this place. Thank you.

Contents

1 Introduction **17**

1.1 Specific Aims 18

1.2 Optics 18

1.3 Microfluidics 21

1.4 Microfabrication of Glass 22

1.4.1 Glass 23

1.4.2 Processing 23

1.5 Design Considerations 24

1.5.1 Single outlet vacuum driven 26

1.5.2 Potential for Lab-on-Chip Integration 26

1.5.3 Diffusivity 27

1.6 Terminology 28

2 Design and Fabrication **31**

2.1 Software Selection and Verification 31

2.2 Velocity Profiles 34

2.3 Flow layering 38

2.4 Flow Tuning 42

2.5 Mask Design 44

2.6 Chip Fabrication 50

3 Experimental Results **53**

3.1 Setup 53

3.2 Initial Observations 55
3.3 Flow Tuning 59
3.4 Stability, Repeatability and Trends 62
3.5 Conclusions 66

4 Discussion and Conclusions **71**
4.1 Accuracy of CFD Modelling 71
4.2 Chip Design and Future Applications of Flow Tuning 74

A Experimental Flow Profiles **77**

B Etch Depth-Dependent Simulated Profiles **85**

C Line Width-Dependent Simulated Profiles **89**

D Simulated 3-Sheath Uncorrected Flows **93**

E Simulated 3-Sheath Corrected Flows **97**

F Sample ADINA Code for Corrected Flow Model **103**

List of Figures

1-1 Diagram of the geometry associated with a collimated beam of light passing through a lens. 19

1-2 A schematic representation of typical hydrodynamic flow (a) and vertical hydrodynamic flow (b). 22

1-3 Diagram of the fabrication process. (B. Mckenna, 2006) 25

1-4 An SEM image of a sectioned channel. (B. Mckenna, 2006) 25

2-1 T-junction. 33

2-2 Mesh density (left) and velocity stability (right) for pressure-driven flow through a simple channel. This is a top-down view of a 40-micron wide channel etched 20 microns deep. From top to bottom: 20, 15 and 5 micron mesh element divisions. 33

2-3 Simple junction with fluids enter from the top and left and combining to exit from the bottom. (a, b) Imaris processed projections of PerkinElmer images. (c) ADINA simulation of particle traces. (d) Coventor simulation of fluid concentration (Keiji Yano, 2006). 35

2-4 (a) Side view of parabolic axial flow. (b) Front view of a Z-direction velocity contour map in a cross section of fully developed flow. The red in the center is approximately 160 microns/sec. The green is approximately 80 microns/sec. The blue is approximately 10 microns/sec. 36

2-5 Side view of velocity vectors at a junction. 37

2-6 Velocity in the sheath channel. Flow in the analysis channel is towards the top of the page. (a) Velocity vectors in the sheath channel at -50 microns. (b) Velocity contours in the sheath channel. The x-direction (top) and y-direction (bottom) contours are shown with individual scales with both positive and negative values. 37

2-7 Focusing schematic. Sheath channels run in the x direction underneath the analysis running in the y direction. The features illustrated on the end of the sheath channels are velocity boundary conditions which were used to regulate flow rate. 39

2-8 (a) Traces placed in the sample sheath channel and tracked downstream through the analysis channel. (b) Angled view of a first attempt at vertical hydrodynamic focusing simulation. The analysis channel had 100-micron etch depth and 40-micron line width. The sheath channels had 75-micron etch depth and 40-micron line widths. Flow rates are approximately 50% Sheath 1, 10% Sheath 2, and 40% Sheath 3. . . . 39

2-9 (a) Front view of the analysis channel showing profiles for identical analysis and sheath channels at sheath flow rates of 10, 30, 50, 70 and 90%. 40

2-10 100-micron vs 60-micron etch depth with line widths of 40 microns. The left half of the analysis channel shown is a progression of profiles of increasing flow rate (10, 13, 50, 70 and 90%) into the analysis channel from a sheath channel etched to 100 microns deep. The right half is an identical progression from a sheath channel etched to 60 microns deep. At 10% the 100-micron profile (lower-left) is steeper than the 60 micron profile (lower-right) but at 90% the 60-micron profile (upper-right) is now steeper than the 100-micron profile (upper-left) 40

2-11 100-micron vs 180-micron etch depth with line widths of 40 microns. The left half of the analysis channel shown is a progression of profiles of increasing flow rate (10, 13, 50, 70 and 90%) into the analysis channel from a sheath channel etched to 100 microns deep. The right half is an identical progression from a sheath channel etched to 180 microns deep. At 30% the 100-micron profile (left, second from bottom) is noticeably shallower than the 180 micron profile (right, second from bottom) but at 90% the profiles (top) seem to be almost equal with the 180-micron profile even being slightly higher in the middle. 41

2-12 60-micron vs 180-micron etch depth with line widths of 40 microns. The trends of etch depth versus the control geometry shown in Tables 2-10 and 2-11 are even more pronounced when compared to each other. 41

2-13 40-micron vs 165-micron line width for a constant etch depth of 100 microns. The 165-micron line width (right) has a more pronounce curvature that struggles to close the gap in the center even at 70%. . 42

2-14 Variations of focused flow. 43

2-15 Tuned flow. Three sheath channels to the left introduce flow and the wider channel on the right removes flow. The bulk motion of the fluid in the analysis channel is still downstream along the z-axis. Two lines of trace markers used to trace the flow upstream and downstream through the 4th junction. 44

2-16 Subtraction junction of line width 150-micron and etch depth 100-micron. (a) Markers placed downstream of the junction and then traced upstream. The uppermost profile is just before the junction and the lower, more complicated ones are upstream beyond the addition junctions. (b) Markers placed upstream of the junction and then traced downstream through to the exit of the analysis channel. 45

2-17 Addition junction of line width 40-micron and etch depth 100-micron. (a) Markers placed downstream of the junction and then traced upstream. The resulting profile is similar to that of the previous figure except less pronounced. (b) Markers placed upstream of the junction and then traced downstream through to the exit of the analysis channel. 45

2-18 Trace (E) placed after Junction 2 (B) 15 microns above the bottom of the channel to mark Sheath 2 flow. As it passes through Junction 3 (C) it is focused upward and inward into a gull wing profile. As the traces pass through Junction 4 (D) they are preferentially pulled downward and outward. The relatively flat layer of traces that is formed is approximately 20 microns higher than where the original traces were placed. 46

2-19 Pattern for inlet channels on the left hand side. Single port outlet on the right hand side. Focusing, tuning and scan regions in between. . . 46

2-20 Eight-lane pattern. Black and red denote top and bottom halves of the chip. 24 inlet wells. One outlet port. 49

2-21 A fabricated chip using the mask patter shown in Figure 2-20. 49

3-1 Top Down view and cross section of a junction. (a) The vertical channel is the analysis channel and the horizontal channels is the analysis channel. (b) An image stack showing the full geometry of the cross section. 56

3-2 Junctions 3 (a) and 4 (b) of Lane D. The fabricated chip was such that even in Lane D, the lane with the most correction, there was no noticeable change in the flow profile. 57

3-3 One millimeter holes drilled into the correction channels to provide greater correction at approximately 30%. 57

3-4 A single confocal slice at a junction with analysis channel flow going left. Light debris build-up (circled) can be seen shortly after the junction. 58

3-5 Bead resolution. A length marker was placed beside a blurred image of a stationary 1-micron bead showing approximate vertical resolution of 4 slices or 11 microns. 58

3-6 Overlaid three-sheath profiles of Lanes F, D and B. This figure is to demonstrate the difficulty of directly comparing profiles in the same manner that was done for ADINA models. The uncertainty in the . 66

4-1 ADINA simulation with revised geometry of Lane H based on experimental measurements. A half-profile of flow after passing through the correction junction subtracting 30% of the flow, the approximate value after diamond-drilled short circuits. 72

4-2 ADINA simulation with the designed geometry of Lane H etched to 100 microns corrected 30% in Junction 4. These are the same flow rates shown in Figure 4-1 except with the original intended geometry. 72

4-3 X-Y view of Lane H with the fabricated geometry. Tracers placed 15 microns from the bottom before the Sheath 3 junction (d) and allowed to pass through the correction junction. (a) Profile after 70% addition at Junction 3. Profile after correction at two different subtraction percentages: (b) the original 17% and (c) twice the amount at 34%. With this geometry, the effects of correction are minimal and even doubling the amount of correction does little to affect the gull wing profile. 72

4-4 Y dependence of flow correction. (a) Horizontal tracers were placed at y = 55 and 65 microns prior to the correction junction. (b) Post-correction, the minimum separation at the middle of the channel has grown to greater than the original 10 microns, demonstrating that correction is also y-dependent. 73

4-5 Demonstration of nonsymmetric profiles. Horizontal tracers were placed 15 microns from the bottom and allowed to pass through two junctions. At some point, symmetric tracer pairs experience different flow conditions caused by a difference in meshing and that error continued through the life of the trace. 74

4-6 Future Design A. Eight lanes with identical flow rates brought to a single imaging window of width 8 mm for easy multi-lane scanning. . 75

4-7 Future Design B. The same concepts can be applied to flow focused from a single side of the analysis channel. Symmetry is lost so the profile may be harder to correct but this format allows for a wider range of percentage flow rates of the sheaths. 75

4-8 Future Design C. If multiple parallel lanes are not necessary, then one larger channel can be designed for a more efficient use of space. Flow can be high-speed before the analysis channel expands. Multiple correction channels progressively correct the vertically focused flow as it is expanded and slowed down. 76

List of Tables

1.1 Minimum spot size and depth of field for values of a typical microscope system. Note that in this hypothetical system a change in depth of field of 10 microns (approx. 30%) results in a 3x improvement in resolution. 21

1.2 Fabrication materials. 26

1.3 Diffusivity of common solutes. 28

1.4 Diffusion of 1-μm diameter spheres in water across microchannels of diameter 100 μm. The Peclet number expresses the relative importance of convection to diffusion. Generally speaking, the Peclet number in the table can be thought of as the number of channel widths required for complete mixing in a channel where bead solution and water are brought together, each initially occupying half of the flow. 28

2.1 Flow ratios for each of the 8 lanes. 48

3.1 Setup specifications 55

3.2 Flow profile sequence of corrected flow in Lane H. 60

3.3 Flow profile sequence of corrected flow in Lane A. 61

3.4 Flow profiles for Lane H. 63

3.5 Consecutive images of the same flow were taken to illustrate the noise in measurement independent of time. 64

3.6 Two-sheath flow. Increasing percent Sheath 2 from top to bottom. . . 65

3.7 Three-sheath flow. Increasing percent Sheath 3 from top to bottom. In (400, B) Sheath 1 had a bubble in the junction so that Sheath 3 is likely to be flowing at closer to 90%. 67

3.8 Three-sheath flow. Increasing percent Sheath 2 from top to bottom. . 68

A.1 Flow profiles for Lane A. 78
A.2 Flow profiles for Lane B. 79
A.3 Flow profiles for Lane C. 80
A.4 Flow profiles for Lane D. 81
A.5 Flow profiles for Lane E. 82
A.6 Flow profiles for Lane F. 82
A.7 Flow profiles for Lane G. 83
A.8 Flow profiles for Lane H. Shown with negative images to contrast what was shown in the Results section. 84

B.2 Profiles of flow from varying etch depth and flow rate of Sheath 2. . . 86

C.1 Profiles of Sheath 2 flow when varying the line width of Sheath 2 for a constant 50% flow rate. 90

D.1 Simulations for uncorrect flows based on lane designs. 94

E.1 Corrected flow simulations based on lane design. Top left: uncorrected. Bottom left: corrected. Right: overlayed. 98

Chapter 1

Introduction

This section is meant as an introduction to the specific goals of the research, general context of the motivations behind this endeavor, and terminology used in the discussion throughout[1]. While the idea of using vertical hydrodynamic focusing to enhance optical resolution in a high-throughput device is unique, there has been a great deal of progress made in understanding many related and critical areas to this project [15]. Flow in microchannels has been characterized for pressure driven [16], electro-osmotic, electro-kinetic [13], and various other types of actuation. Hydrodynamic focusing has been coupled with mechanical actuation [11] for flow switching and optical actuation for particle or cell sorting [19] . Polydimethylsiloxane (PDMS) is the material of choice for prototyping of most microfluidics [12] and glass is also used [5] as it is a more stable and generally more useful for commercial devices. Microfluidic flows have been focused to contain droplets [18], cells, dyes , and other solutes. Microfluidic flows have been imaged, sometimes confocally [8], to study diffusion [7], mixing [17], material formation [2], and other phenomenon [9]. Vertical hydrodynamic focusing has even been done before in more complicated PDMS devices [20, 14] but not the same methods available for and used in this project.

[1] Although not necessary, many figures have been enhanced with color so it is suggested that this document be viewed in color.

1.1 Specific Aims

The primary goal of this project was to create an isotropically etched microfluidic chip capable of vertical hydrodynamic focusing for improved imaging conditions of microfluidic flow. The chip was to be made out of bonded glass because of its excellent optical, chemical and biological properties, and the design was to be kept as simple as possible to allow for the possibility of a future scale-up to a highly parallel implementation for high throughput. In the past, literature about hydrodynamic focusing has focused on other aspects such as droplet formation, flow switching, material deposition, or molecular kinetics. The challenge of this project was to overcome the limited geometries of glass fabrication and demonstrate a technique applicable to a wide variety of application requiring hydrodynamic focusing.

1.2 Optics

Many things that are being studied in biology, chemistry and engineering occur on the micrometer scale. It can be difficult to miniaturize instruments to fit inside these micron-sized environments so optical devices are often the tool of choice to probe and measure various properties of these tiny systems. Beams of light can be reflected, refracted, superimposed and measured in such a multitude of ways that methods have been developed to use light to determine many physical properties, structures and interactions of living and non-living objects. As with most measurement systems, the performance of an optical system is often thought of in terms of resolution and speed. How small of an object can be distinguished? How many at a time or how often can this happen?

The resolution of a lens is commonly defined by a minimum spot size, D_{airy}, determined by the lens geometry and the type of light used. A plane wave of light passing through a circular aperture creates an intensity profile modeled by the Bessel function. An Airy disc is the central bright region surrounded by subsequent rings of intensity, each separated by a circle of zero intensity. D_{airy} is the diameter of the first

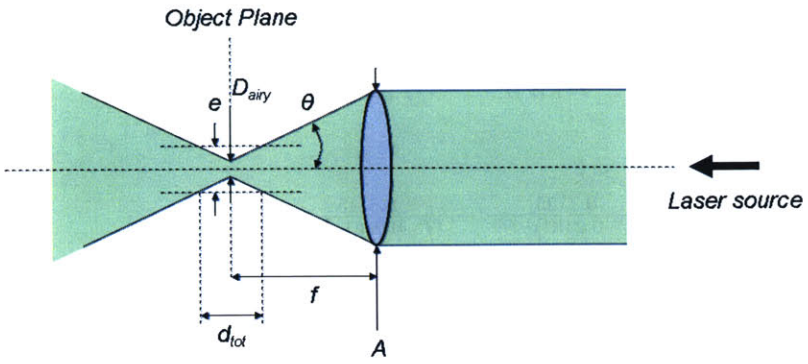

Figure 1-1: Diagram of the geometry associated with a collimated beam of light passing through a lens.

zero-intensity circle surrounding the Airy disc and defined as the diffraction-limited spot size [6].

$$D_{airy} = 2.44 \times \lambda \times f\#$$

or

$$D_{airy} = \frac{2.44 \times \lambda}{2 \times NA}$$

λ is the wavelength of the light. $f\#$ or f-number is a geometrical measure describing the cone angle of the rays passing through the lens. It determines the brightness of the image, depth of field, and the resolution of the lens. A smaller f-number collects more light, has better resolution, and has a smaller depth of field. Another geometrical measure containing the same information is the numerical aperture of the lens, NA.

In laser optics, the distribution of light is more correctly described by a Gaussian profile with the defined diameter being taken as the full-width half-maximum, FWHM, value of the intensity distribution. In this case, the leading coefficient of the previous equation is replaced by a variable determined by T, the ratio of the FWHM Gaussian beam diameter to the limiting aperture diameter.

$$D_{FWHM} = K_{FWHM} \times \lambda \times f\#$$

$K_{FWHM} = 1.029 + \frac{0.7125}{(T-0.2161)^{1.821}} - \frac{0.6445}{(T-0.2161)^{2.221}}$

$T = \frac{D_b}{D_t}$

$f\# = \frac{f}{A}$

$NA = \sin\theta_{cone}$

$f\# \approx \frac{1}{2 \times NA}$

While the minimum spot size describes resolution in the focal plane of the lens, the position of the object of interest along the primary axis of the lens is also very important to the resolution of the system. This is know as the depth of field of the object. As an object deviates from the focal plane, the spot size that it is imaged with increases and reduces the resolution of the system. The formula for calculating depth of field, d_{tot}, for a desired resolution, e, is shown in the following equation. n is the refractive index of the medium between the lens and object. This is usually air ($n = 1.00$) or immersion oil ($n = 1.52$). The first term in the formula accounts for the Gaussian propagation of a beam of light and the second term is for the geometry the lens [6, 3].

$$d_{tot} = \frac{\lambda \times n}{NA^2} + \frac{n}{NA} \times e$$

Having defined a minimum spot size, another measure of resolution is the Rayleigh criteria which states that the maximum resolution occurs when the maxima of the Airy disk from a point source overlaps the first minima of the Airy disk of second source. Using this definition, the best resolution is one half the minimum spot size. Common values of the mentioned parameters are shown in Table 1.1.

Parameter	Value
20x lens	$NA = 0.2$
Argon-ion laser	$\lambda = 488$ nm
for $T = 1.0$	$K_{FWHM} = 1.13$
Air	$n = 1.0$
Minimum spot size	$D_{FWHM} = 1.38\mu m$
Rayleigh resolution	0.69 μm
Depth of field for a desired resolution: $e = 3\mu m$	$d_{tot} = 27.2$ μm
Depth of field for a desired resolution: $e = 1\mu m$	$d_{tot} = 17.2$ μm

Table 1.1: Minimum spot size and depth of field for values of a typical microscope system. Note that in this hypothetical system a change in depth of field of 10 microns (approx. 30%) results in a 3x improvement in resolution.

1.3 Microfluidics

For chemical reactions, material formation from aqueous solutions, cell functions, and other processes that occur in a liquid environment, microfluidics are a convenient environment for manipulation. The always laminar flow conditions in microfluidics can be exploited to give highly predictable and reproducible experimental conditions. Transport occurs only by diffusion so precise tracking and manipulation of particles in flow are also possible in these conditions.

Hydrodynamic focusing is a technique that utilizes laminar flows to bring different streams of fluid together to isolate one fluid from another or from its environment. Fluids of different properties or containing different compounds can be sandwiched together to form layered flow that will remain layered, except for diffusion of small particles or molecules, because of the laminar flow conditions. Each layer's composition is dependent on that layer's original composition and the diffusion effect from its neighbor. If operating in a diffusion-limited environment, then thickness of the layers controls how quickly each will reach equilibrium. The benefits of microfluidics and hydrodynamic focusing have been demonstrated in numerous devices for DNA analysis, flow cytometry, microreactors, molecular kinetics, and other lab-on-chip applications [10].

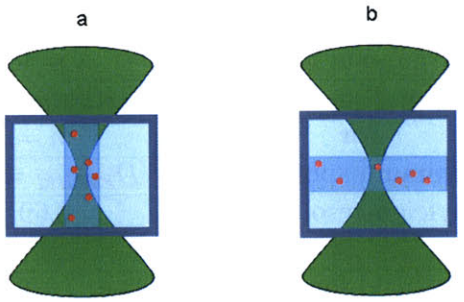

Figure 1-2: A schematic representation of typical hydrodynamic flow (a) and vertical hydrodynamic flow (b).

Because of the nature of microfabrication, most hydrodynamic focusing has been done horizontally. The focused sheath of fluid is typically perpendicular to the plane of the device and parallel to any optical imaging axis. This does nothing to confine the layer of interest into the depth of field of the imaging system.. Our goal was to provide vertical focusing to constrain the central sheath to a narrowlayer, all constrained within the depth of field. As shown in Table 1.1, if a flow occupying 27 microns in vertical height were reduced to 17 microns, the resolution that could be achieved would be improved by three-fold. Even for applications without the need for high resolution, vertical hydrodynamic focusing could still allow for cleaner signal collection for the same detection geometries by forcing particles to pass by the sensor in a single layer, preventing signal contamination from multiple objects being read as one. Hydrodynamic focusing was developed as a way to control nanloliter-sized environments, and vertical hydrodynamic focusing is a way to improve the optical signal performance of those focused environments.

1.4 Microfabrication of Glass

Machines and techniques borrowed from the semiconductor industry are the workhorses of microfluidic device fabrication. The adoption and adaptation of these tools into microfluidics has allowed for the precision production of nanoliter-volume devices. The

evolution of these tools and techniques continues to provide a rich breeding ground for the creation of new microdevices for new applications.

Microfabrication is a very useful tool when the things that are being studied are happening on the scale of microns. Bench top experiments may be quicker to set up but offer bulk, averaged information and little control of the microscopic environments. Microdevices do not operate with the same volumes as traditional experiments which can be a either a good or bad thing but if necessary, microdevices which start as a single device the size of a microscope slide can often be scaled up to hundreds of parallel devices on a single glass device [1] to get closer to traditional volumes.

1.4.1 Glass

The properties of glass have made it a choice material over a broad range of uses. Contaminants can be cleaned off using harsh chemicals because of its stability in many corrosive environments. Depending on the detailed composition, glass is optically transparent from the ultraviolet wavelengths ($\sim$190 nm), through the visible spectrum and into the infrared ($\sim$10 μm) . It has long been used in biology because of its biocompatibility and low absorption. A wide range of surface chemistries have been developed to activate or passivate it for various applications. Glass can be used in temperatures well below 0 °C and well above 100 °C, and microchannels made in glass can withstand hundreds of PSI in pressure if fully bonded. Glass is also a good for electrical isolation for application such as electrophoresis and electro-osmotically driven flow.

1.4.2 Processing

With solution-based "wet" process, the etching is generally an isotropic process, i.e. the glass is etched equally in all directions. The depth of a trench cannot be controlled completely independent of its width. To create an enclosed channel, the etched surface of one plate is bonded to the etched surface of another plate. The intersection of trenches can be controlled by how they are aligned but when they cross, the empty

volume of the trenches are joined because a channel cannot be formed on one plate independent of the other plate.

In our process, access to the channels is achieved by laser-drilled holes. This process is done before the bonding of the two halves because the relatively poor control of laser ablation depth and because laser ablation of the glass creates debris which can be removed before bonding. Once the two halves are bonded, fittings can be attached to the chip to provide access to the channels through the laser-drilled holes. If necessary, a large chip may then be sectioned off into smaller chips by a diamond saw or some other method.

Conventional fabrication of silicon wafers in the semiconductor industry uses many of the same processes but for a different end product. Some key differences are the depth to which the glass is etched and the bonding of two pieces to create a channel. In typical semiconductor processing, silicon dioxide ("glass") is usually a layer that is deposited or grown on top a bulk material, single crystal silicon. The single crystal silicon is resistant to the etchant so when exposed silicon dioxide is eaten away, the process essentially stops. For fabrication of microfluidic devices, glass is the bulk material and the etch process is not simply to expose something underneath the glass but to remove a certain amount of it. While typical semiconductor process remove angstroms or a few microns of glass, the processes used for microfluidic devices sometimes remove a few hundred microns of material. In semiconductor fabrication layers are usually created by deposition or growth through chemical reactions so the glass bonding process one that is more unique to microfluidic devices.

1.5 Design Considerations

Beyond the the details of the specific aims, optics, microfluidics, and fabrication, there were a few additional factors to be considered in how an actual device would be applied and operated.

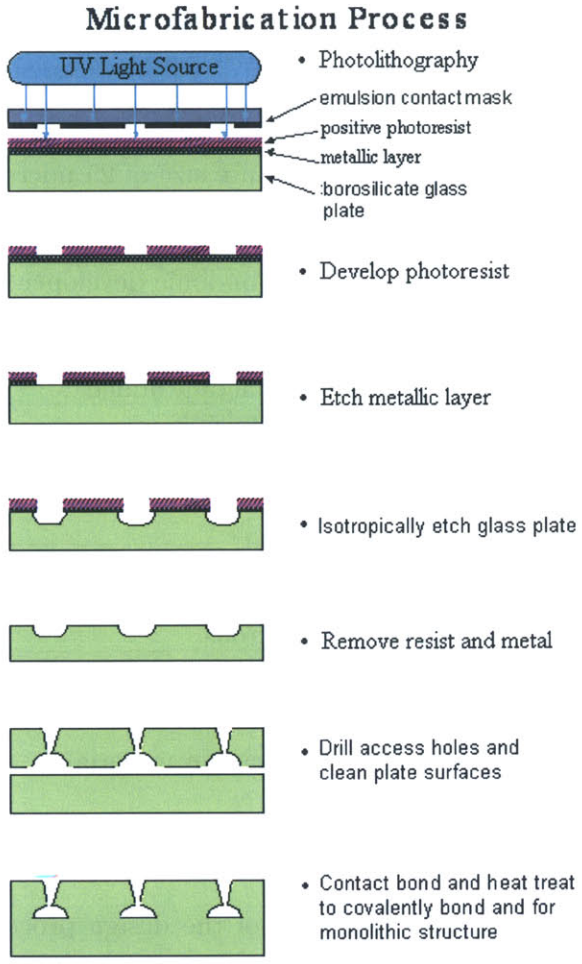

Figure 1-3: Diagram of the fabrication process. (B. Mckenna, 2006)

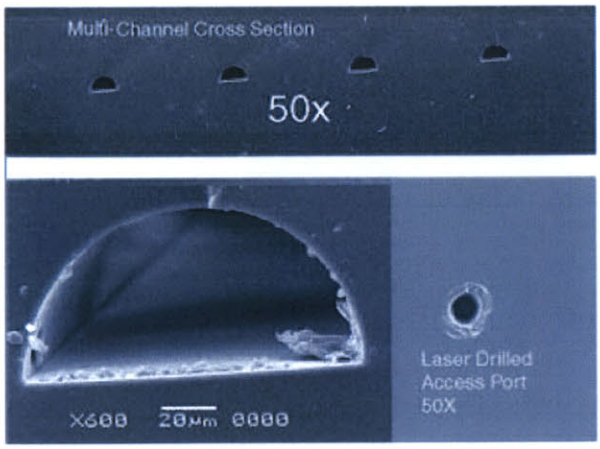

Figure 1-4: An SEM image of a sectioned channel. (B. Mckenna, 2006)

Glass Plate	10" x 5" x 0.7 mm Corning Eagle substrates with chrome and 10, 000 angstroms of AZ1518 photoresist	Telic Company Valencia, CA
Transparency Mask	Emulsion mask printed with a laser photoplotter Minimum feature size of 25 micron 1/8 mil (~3 micron) resolution	Advanced Reproductions North Andover, MA or PageWorks Cambridge, MA
Photoresist Developer	CC-300.40S Non-ionic developer	Cyantek Corporation Fremont, CA
Chrome Etchant	CR-14S Chromium Photomask Etchant - Surfactant added	Cyantek Corporation Fremont, CA
Glass Etchant	Buffered Oxide Etch - 25% hydrofluoric acid - 7% nitric acid - 68% water	Sigma-Aldrich St. Louis, MO
Port Holes	Laser-drilled holes Minimum diameter of approximately 80 microns	Laser Services Inc Westford, MA
Chip Sectioning	Diamond saw	OPCO Labs Fitchburg, MA

Table 1.2: Fabrication materials.

1.5.1 Single outlet vacuum driven

Simplicity and scalability were two goals of the design process, and it was decided early on to build a device to be actuated with a single mechanism at a single node on the chip. A syringe pump (volumetric flow) was selected over electrically driven flow and pressure driven flow. Compared to electrically driven flow, a syringe pump can operate over larger range of flow conditions and is more compatible with live-cell biological imaging. In terms of collecting data from a device, volumetric flow rate, or velocity, is more relevant than pressure, so therefore a syringe pump gave more direct control over a relevant parameter.

1.5.2 Potential for Lab-on-Chip Integration

Simplicity was also emphasized because of the potential of integration for lab-on-chip applications. An imaging device by itself can provide meaningful information but the preparation that happens before and the actions that happen after are also very

important and in many cases could also benefit from miniaturization. Integration with other devices was not a goal of this project but was definitely considered for future applications. For example, a four-component lab-on-chip device could have a bioreactor to culture living cells, an imaging window to identify certain cells, a sorting mechanism, and a polymerase chain reaction region to analyze DNA. The complexity of an integrated system such as this can grow exponentially with the complexity of each of its components. A simple component may not integrate into a system for various reasons but a complex component most certainly cannot be integrated into a system.

1.5.3 Diffusivity

When dealing with particles in space and time, diffusion is always a concern and is especially relevant to microfluidics since there is no turbulent mixing. The diffusivity of a spherical particle in solution is shown below along with a table values for some common particles. In testing conditions, a 1-micron polystyrene bead was suspended in a 50% glycerin/50% water solution (5 times the viscosity of water [4]). Under these condition, it would take a bead on average 7 minutes to diffuse 10 microns. For an average velocity of 350 microns/second a bead in our device would need to travel 16 centimeters. In the tested device, the maximum distance a focused stream would need to travel to the optical window is 3 cm. Diffusion in the experimental setup was negligible, especially when considering the resolution of the imaging [15].

Approximate diffusivity, D, of a spherical particle in solution with diameter a:

$$D \approx \frac{k_b T}{6\pi\eta a}$$

Approximate time, t, required for a particle with diffusivity D to travel a length w:

$$t \approx \frac{w^2}{D}$$

	Dynamic viscosity, μ, N-m/s^2		
Water @ 20°C	0.001		
	Diameter, a, μm	Diffusivity, D, μm^2/s	Time, t, in minutes for 10 μm travel
Small protein	0.005	40	0.039
1-μm bead	1.00	0.2	7.8
Cell	10.0	0.02	78

Table 1.3: Diffusivity of common solutes.

volumetric flow rate,μm/hr	avg velocity per channel, μm/s	Peclet Number
100	175	8.2x10^4
200	350	1.6x10^5
400	700	3.3x10^5

Table 1.4: Diffusion of 1-μm diameter spheres in water across microchannels of diameter 100 μm. The Peclet number expresses the relative importance of convection to diffusion. Generally speaking, the Peclet number in the table can be thought of as the number of channel widths required for complete mixing in a channel where bead solution and water are brought together, each initially occupying half of the flow.

1.6 Terminology

- A **plate** is the initial material used at the start of the microfabrication process up until it is bonded with another plate. It is a borosilicate sheet of glass measuring 254x127x0.7 mm.

- A **chip** is a functional microfluidic device made of two bonded plates and attached ports. There are multiple lanes and channels on a chip.

- A **lane** is a set of channels on a chip capable of hydrodynamic focusing.

- A **channel** is formed when two plates are bonded to enclose the etched surfaces of the plates.

- **Chrome** is deposited as a thin layer of metal on top of the glass plate and resistant to the solution used to etch the glass. It is completely removed by the end of microfabrication.

- **Photoresist** is a photoreactive polymer layer on top of the chrome used for microfabrication. It can be patterned by ultraviolet light and is resistant to the solution used to etch the chrome.

- **Emulsion mask** is an opaque 2-D design printed on a transparency used to preferentially expose the photoresist to ultraviolet light.

- **Depth of field** is a parameter of the lens defined as the distance along the primary axis given acceptable amount of blur. During this paper it often used in a different context as the distance occupied by the sample of interest along the primary axis of the lens. For a smaller distance, all of the objects in the sample can be imaged at a better resolution. This is just a difference in terminology of whether resolution determines depth of field or vice versa.

- **Hydrodynamic focusing** is the use of moving liquids to create layers of different fluids often used to isolate or sandwich a layer of particular interest .

- **Vertical hydrodynamic focusing** is focused flow where a layer is confined vertically. In a cross-sectional view the layer would be horizontal.

- A **junction** is a perpendicular intersection of two channels.

- The **analysis channel** the focused sample of interest and flows past the imaging window analysis.

- **Sheath 1** is the first fluid to enter the analysis channel at Junction 1.

- **Sheath 2** is second fluid to enter the analysis channel at Junction 2 and combines with sheath 1. Sheath is also known as the sample sheath or the focused sheath.

- **Sheath 3** is third fluid to enter the analysis channel at Junction 3 and combines with Sheaths 1 and 2.

- The **sample sheath** is the sheath focused between Sheaths 1 and 3 and typically contains the imaged objects.

- **Percent flow** refers to the percentage of volumetric flow rate in the analysis channel contributed by a certain sheath layer.
- **X-axis** is the axis transverse to the analysis channel.
- **Y-axis** is the axis normal to the outer surface of the chip and parallel to the primary axis of the lens. It can also be thought of as the vertical direction.
- **Z-axis** the axis parallel to the analysis channel. The bulk motion of the fluid is in this direction.
- An **image stack** is a 3-D image comprised of a series of 2-D images taken with a confocal microscope at a constant interval in the y-direction (vertical).
- **Bead concentration** is the volumetric percentage of bead solution normalized to an unknown absolute initial concentration.
- **Dye concentration** is the molar concentration of fluoresceine dye.

Chapter 2

Design and Fabrication

The resulting problem is steady state, three dimensional, incompressible and does not exhibit symmetry about any axis. Rather than approach the Navier-Stokes equations analytically, it was decided to take advantage of the numerous commercial computational fluid dynamics (CFD) packages available. With the aid of CFD software, a range of flow conditions in our microchannels was simulated. Through these analyses and observations, a chip for vertical hydrodynamic focusing was designed using the unique profiles generated at the junctions of channels and their dependence on flow rate and geometry.

2.1 Software Selection and Verification

Initial testing of simulation software resulted in stable solutions of microfluidic channels and T-junctions (2-1) and experimental imaging techniques were developed to characterize flow in a real chip to validate the simulations. A trial installation of Coventor [1] was used initially and mixing (Figure 2-3(d)) and velocity profiles were created from the simulations. Later, a trial version of ADINA [2] was installed and further simulations were run to test particle traces and meshing (Figure 2-2). A full

[1] CoventorWare 2006, Coventor, Inc., Cary, NC

[2] ADINA (Automatic Dynamic Incremental Nonlinear Analysis), ADINA R & D, Inc., Watertown, MA. Special thanks to Professor K.J. Bathe of the Department of Mechanical Engineering for providing this software package.

version of ADINA was eventually selected as the simulation tool for this research based on cost and availability as a single package rather than multiple modules.

Computational power required for each simulation was a concern because multiple models would be needed to characterize the flow for a range of design parameters. Solution time did not scale linearly with mesh size so the coarsest divisions possible that still yielded acceptable results were used. For example, a model with 19200 nodes required 224 seconds to solve but a model with 26800 nodes (40% increase) required 467 seconds (100% increase) to solve. In order to reduce computing times, models were preferentially meshed with finer elements on the edges of the junctions and coarser elements in regions where simple parallel flow was expected. Even with the biased meshing, occasional abnormal elements resulting from the elimination of sliver or excessively small elements were generated. This could not be completely avoided without reducing the size of all elements in the model so they were accepted and kept in mind when analyzing the results. In general, divisions were never larger than 20 microns and the smallest dimension of the model always had at least 5 divisions. A typical command file used for ADINA is given in the Appendices.

A test chip with a junction geometry identical to the model used in the simulations was fabricated to mimic the T-junctions and typical etch depth expected in a final design. A complementary pair of fluorescent dye and beads were selected and two confocal microscopes, Zeiss LSM 510[3] and PerkinElmer spinning disk, were tested for their imaging capabilities. The speed of the flow and the intensity of the emitted fluorescence were the two primary difficulties in working with the microscopes. The result of this testing showed that the Zeiss had much better y resolution but its laser scanning head was not capable of capturing consecutive 3-D images quickly enough to follow a single bead as it passed through the imaging window ("y" in terms of

[3]This work was conducted utilizing the W.M. Keck Foundation Biological Imaging Facility and the Whitehead Institute

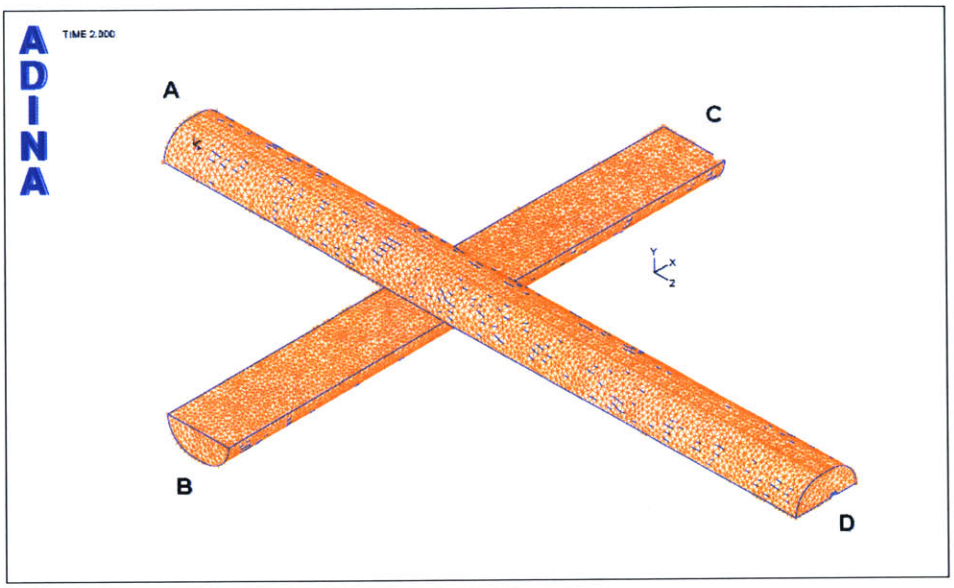

Figure 2-1: T-junction.
Setup for initial software and imaging calibrations: Two inlet flows from A and B . Single outlet flow from C. No flow allowed through D (wall boundary condition). The analysis channel is on top. The sheath channel is on bottom. Percentages of flow from A and B would be in reference to D, the total flow after the junction.

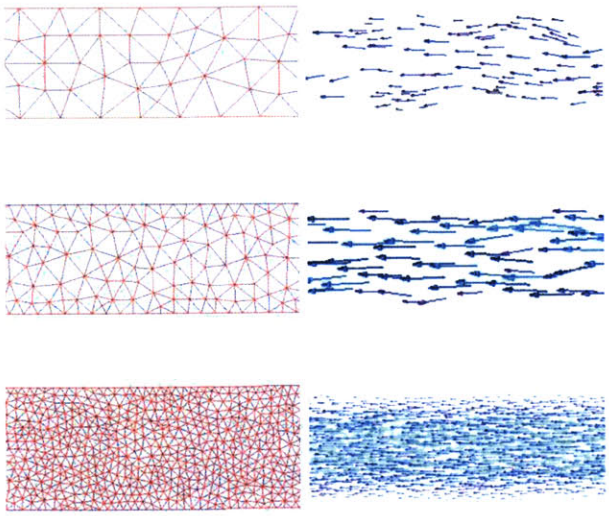

Figure 2-2: Mesh density (left) and velocity stability (right) for pressure-driven flow through a simple channel. This is a top-down view of a 40-micron wide channel etched 20 microns deep. From top to bottom: 20, 15 and 5 micron mesh element divisions.

microscope orientation is the vertical plane in keeping with the microfluidic models). The PerkinElmer with its spinning disk configuration was capable of much faster scan rates so that the path of a specific bead could be captured as it was flowing through the channel; however, the y resolution suffered greatly because of the lack of control over excitation/emission filter pairs and pinhole size. Although the images were not complete, they were sufficient for initial verification of flow profiles. Fig 2-3 shows a projected top down image taken with the PerkinElmer. With the PerkinElmer, it was not possible to resolve z-axis location of the passing beads but the acquired images could be processed with Imaris [4] to eliminate noise and track objects moving through the imaging window. The result was a stroboscopic effect that allowed for tracking bead paths. The projected images of the bead flow and the path lines of the simulations supported each other very well. The LSM 510 had the opposite performance. The y resolution was good enough to create a cross section of the channel but gain had to be turned up to to capture beads flowing by. The increased gain caused a blooming effect from beads which were moving very slowly or stuck on the walls of the channel.

2.2 Velocity Profiles

In analyzing the flow characteristics, a standard channel with 40-micron line width and 100-micron etch depth was used. Models with this geometry served as the control case for each variable tested. Velocity profiles in the pressure-driven semi-circular channels were parabolic as expected. The maximum velocity in the channel was greater than the average velocity by a factor of approximately 1.6. With the isotropic wet etching creating an aspect ratio of about 2:1, it makes sense that this factor would be closer to that of an infinite parallel plate, 1.5, than that of a channel with a circular cross section, 2.0. Figure 2-4 is a contour plot of the z-velocity with the maximum appearing at y = 55. It was important to note the velocity profile because of its impact on the speed, and ultimately throughput, of the sample fluid. Later

[4]Bitplane AG, St. Paul, MN

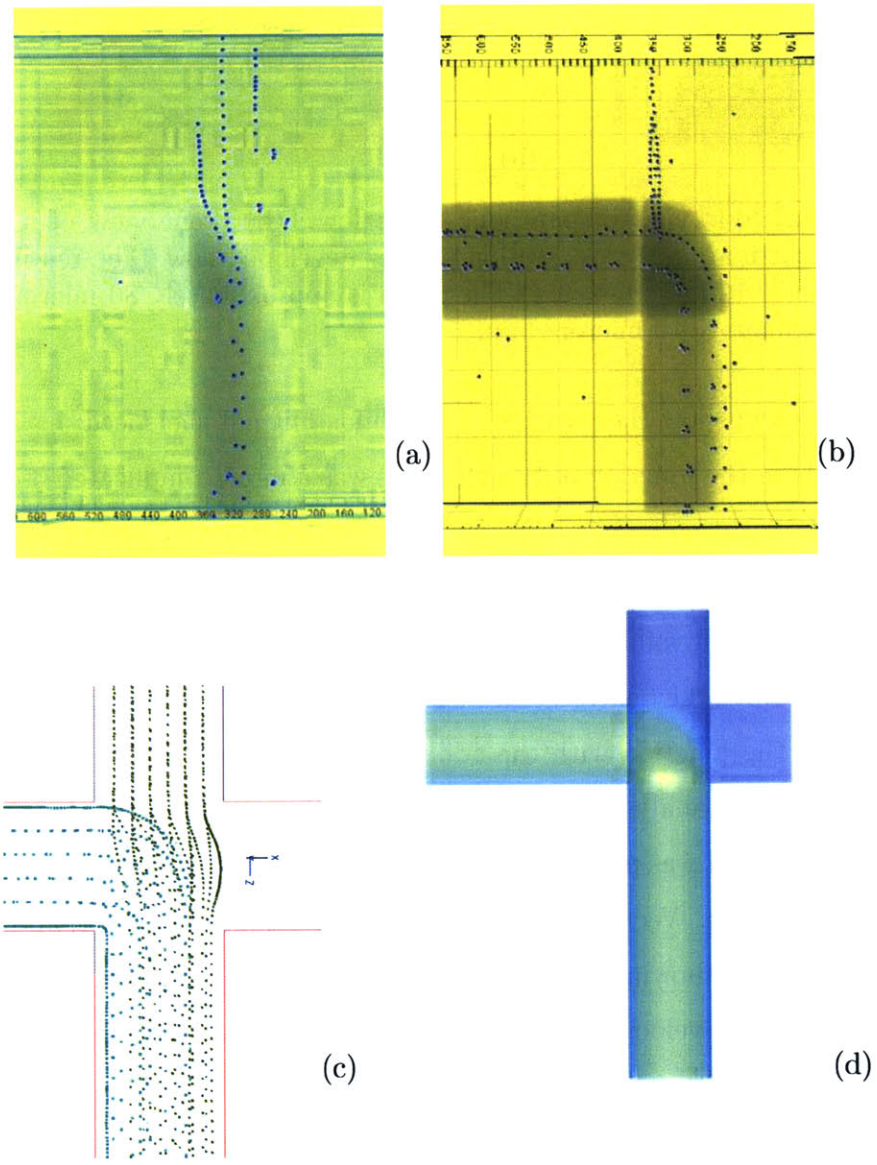

Figure 2-3: Simple junction with fluids enter from the top and left and combining to exit from the bottom. (a, b) Imaris processed projections of PerkinElmer images. (c) ADINA simulation of particle traces. (d) Coventor simulation of fluid concentration (Keiji Yano, 2006).

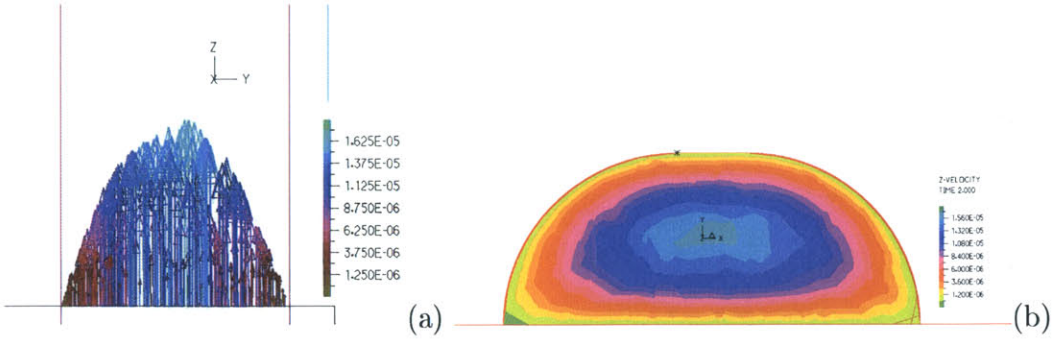

Figure 2-4: (a) Side view of parabolic axial flow. (b) Front view of a Z-direction velocity contour map in a cross section of fully developed flow. The red in the center is approximately 160 microns/sec. The green is approximately 80 microns/sec. The blue is approximately 10 microns/sec.

particle traces will show the location of the fluids but not the speed.

The profile in the junction of two channels was a more complicated 3-dimensional flow with significant components in the x and y directions. The flow added by the sheath channel at the junction created upward and inward velocities. In addition to that, the expansion in volume at the junction created a downward velocity in the first half that drove both the analysis and sheath fluids downward. The contraction in the second half of the junction with the addition of the sheath flow created an upward acceleration into the analysis channel. Using velocity vectors and contour maps along with cutting planes it was possible to see which flows dominate the velocity in different areas of the junction. Vector plots were helpful in visualizing direction and contour plots were good for showing magnitudes. Putting this all together, one can see that there is a downward velocity of the analysis fluid into the sheath channel caused by the added volume of the sheath channel. This volume of fluid is forced inward by the addition of the sheath fluid and eventually all of it is forced upward by the contraction back into the analysis channel.

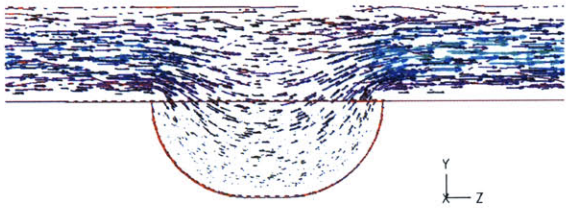

Figure 2-5: Side view of velocity vectors at a junction.

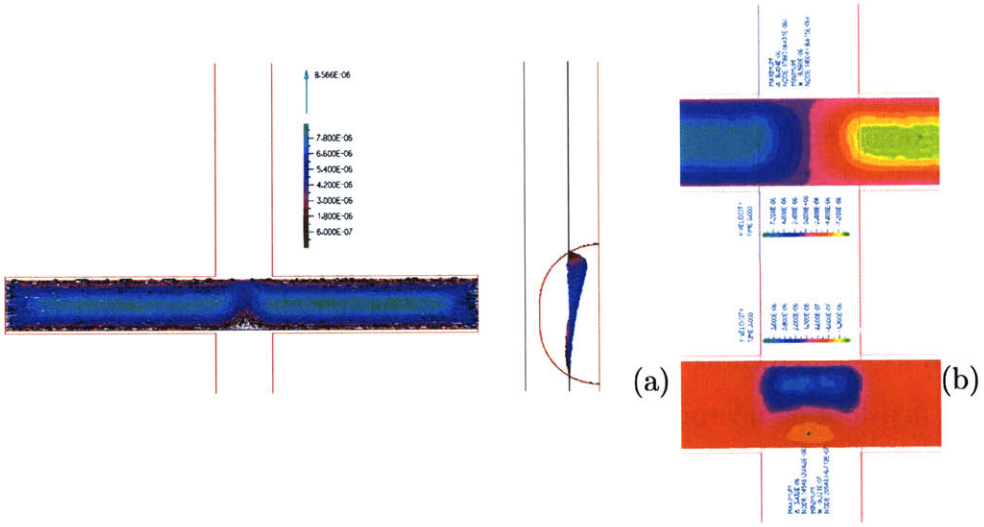

Figure 2-6: Velocity in the sheath channel. Flow in the analysis channel is towards the top of the page. (a) Velocity vectors in the sheath channel at -50 microns. (b) Velocity contours in the sheath channel. The x-direction (top) and y-direction (bottom) contours are shown with individual scales with both positive and negative values.

2.3 Flow layering

In a first attempt to simulate vertical hydrodynamic focusing, three sheath channels were attached to the analysis channel (Figure 2-7) and particle traces were placed in the simulated flow to visualize the layering of the fluids. The results showed a focused sample flow with a sweeping profile that nearly spanned 2/3 of the height of the analysis channel (Figure 2-8). To understand this better the fabrication variables were systematically tested in the simple T-junction. The relative flow rate, mask line width, and etch depth were independently controlled and flow profiles were created for each condition. The analysis channel was kept at the standard 40-micron line width and 100-micron etch depth while the flow rate, line width, and etch depth for the sheath channel were decreased and increased with respect to the analysis channel. The results showed that as flow rate increases, the profile grows inward and upward with a slight maximum in curvature in the range of 50% sheath flow (Figure 2-9). The ability of the sheath layer to close the gap between the two halves of the analysis channel was also a function of the flow rate.

In a similar manner, the relationship between the etch depth and layering profile was explored (Figures 2-10,2-11,2-12). The most noticeable difference in the profiles is the change in the angle at the boundary between the two fluids, measured internal to the incoming sheath fluid. For etch depths less than the analysis channel, the angle of the wedge formed by the sheath fluid is initially smaller than the control case and as the percentage of sheath flow increases so does the boundary angle. For an etch depth of 60 microns, the angle of the sheath flow surpasses the angle for the control case at 50%. For sheath channel etch depths greater than the analysis channel the angle is initially larger than the control case and decreases as percent flow rate increases approximately equaling the control angle at 90% sheath flow.

Varying the line width had a similar effect as etch depth; however, reducing the line width did not create a noticeable difference because the initial control value of 40 microns was already a minor feature of the overall geometry of the channel. Increasing the line with to a value of 165 microns created noticeable changes in angle

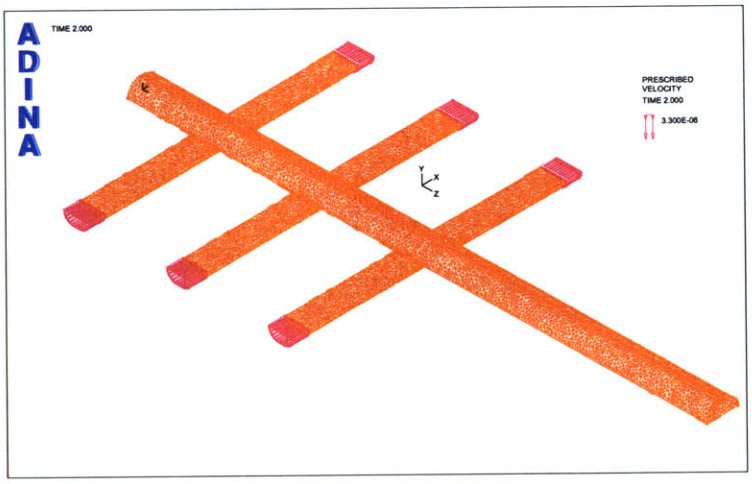

Figure 2-7: Focusing schematic. Sheath channels run in the x direction underneath the analysis running in the y direction. The features illustrated on the end of the sheath channels are velocity boundary conditions which were used to regulate flow rate.

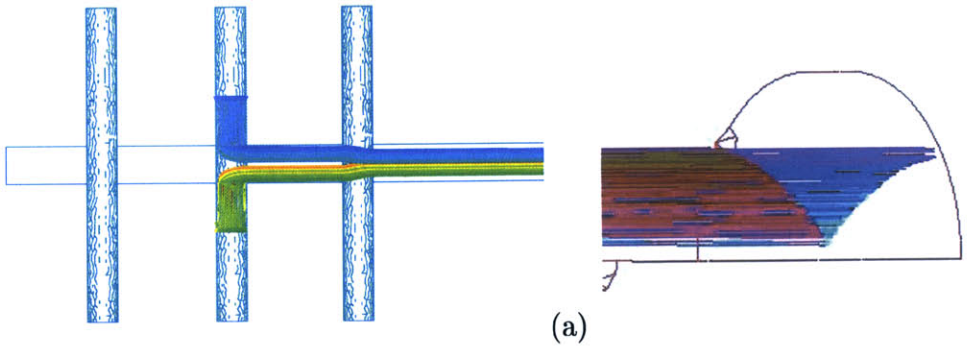

(a) (b)

Figure 2-8: (a) Traces placed in the sample sheath channel and tracked downstream through the analysis channel. (b) Angled view of a first attempt at vertical hydrodynamic focusing simulation. The analysis channel had 100-micron etch depth and 40-micron line width. The sheath channels had 75-micron etch depth and 40-micron line widths. Flow rates are approximately 50% Sheath 1, 10% Sheath 2, and 40% Sheath 3.

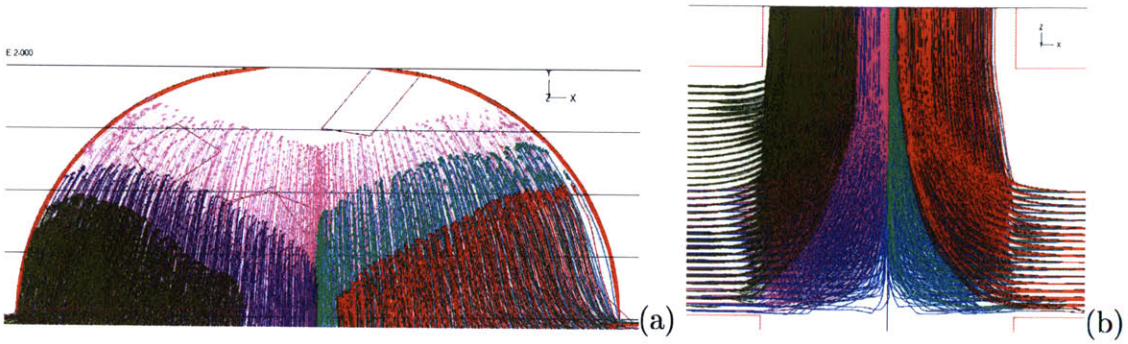

Figure 2-9: (a) Front view of the analysis channel showing profiles for identical analysis and sheath channels at sheath flow rates of 10, 30, 50, 70 and 90%.
(b) Top down view of the junction showing the transition from x-velocity dominated flow to z-velocity dominated flow.

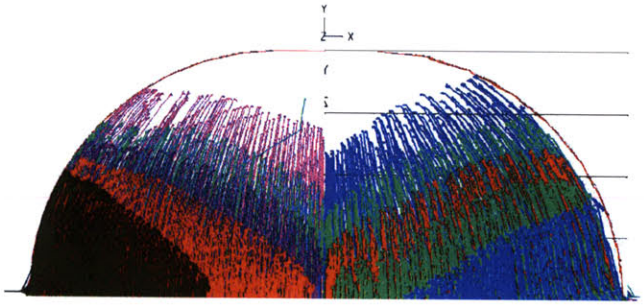

Figure 2-10: 100-micron vs 60-micron etch depth with line widths of 40 microns. The left half of the analysis channel shown is a progression of profiles of increasing flow rate (10, 13, 50, 70 and 90%) into the analysis channel from a sheath channel etched to 100 microns deep. The right half is an identical progression from a sheath channel etched to 60 microns deep. At 10% the 100-micron profile (lower-left) is steeper than the 60 micron profile (lower-right) but at 90% the 60-micron profile (upper-right) is now steeper than the 100-micron profile (upper-left)

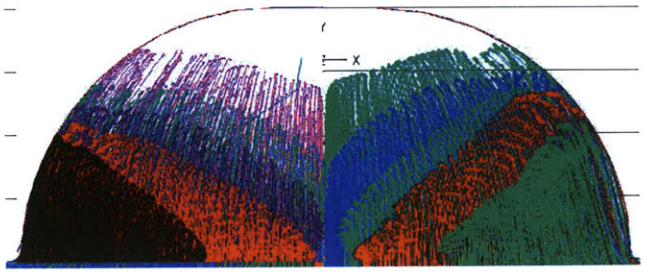

Figure 2-11: 100-micron vs 180-micron etch depth with line widths of 40 microns. The left half of the analysis channel shown is a progression of profiles of increasing flow rate (10, 13, 50, 70 and 90%) into the analysis channel from a sheath channel etched to 100 microns deep. The right half is an identical progression from a sheath channel etched to 180 microns deep. At 30% the 100-micron profile (left, second from bottom) is noticeably shallower than the 180 micron profile (right, second from bottom) but at 90% the profiles (top) seem to be almost equal with the 180-micron profile even being slightly higher in the middle.

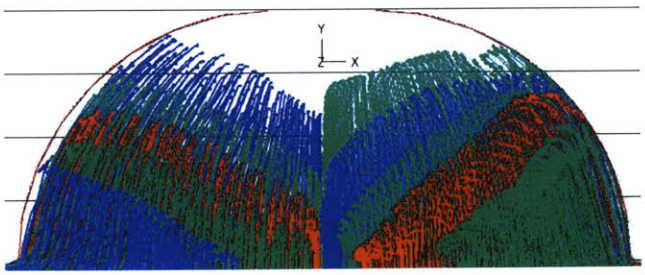

Figure 2-12: 60-micron vs 180-micron etch depth with line widths of 40 microns. The trends of etch depth versus the control geometry shown in Tables 2-10 and 2-11 are even more pronounced when compared to each other.

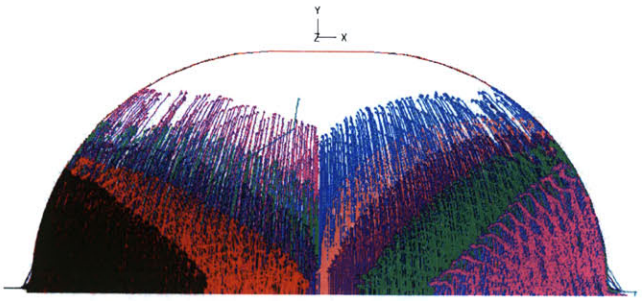

Figure 2-13: 40-micron vs 165-micron line width for a constant etch depth of 100 microns. The 165-micron line width (right) has a more pronounce curvature that struggles to close the gap in the center even at 70%.

from the control channel and more subtle changes than those from increased etch depth showed. As with etch depth, increasing line width created a steeper wedge of sheath fluid at low flow rates. The difference was that as sheath flow rate increased the wedge showed a more pronounced curvature with the two halves not connecting in the middle of the channel until flow rates of more than 70%.

A second try at vertical hydrodynamic flow exhibited the same gull wing characteristics as the first but the variation in height could be reduced by increasing the flow rate of the third sheath layer or using more than 30% for the sample sheath. Maintaining a final sample sheath of 15%, the buffer sheaths were varied to focus the sample sheath to different region of the analysis channel.

2.4 Flow Tuning

The hypothesis reached from the CFD analysis was that the resulting geometry-dependent profiles could be added and subtracted to create a flatter focused profile than addition alone. In this extremely low Reynolds number Stokes' flow regime and especially since the geometry is identical moving upstream and downstream, flow is time independent and the profiles for adding fluid at a junction and removing fluid are identical and depend only on the geometry (and of course flow rate). Simulations in the previous section were of junctions where flows were combined. In the the inverse case of the combining junction's flow field, the result is a junction that separates or

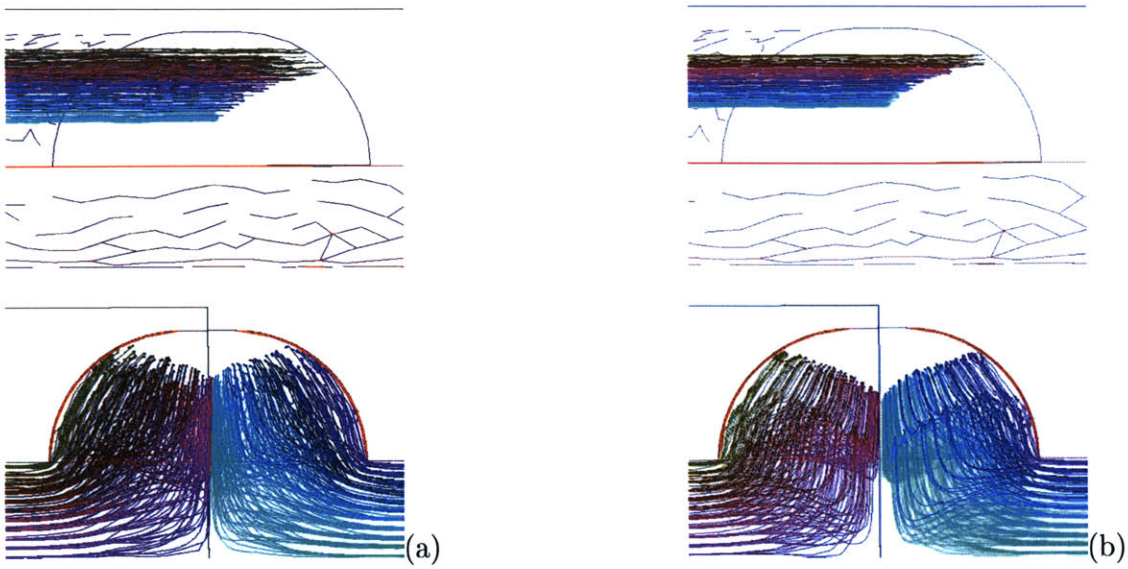

Figure 2-14: Variations of focused flow.

subtracts fluid with the fluid being removed having exactly the same profile as the simulations for additive flow. Starting with a three-sheath flow using the relatively flat control geometry or 60-micron deep sheath channel, flow can then be preferentially subtracted from the outer edges using the higher angle wedge of a 165-micron deep sheath channel. This results in a tuned or corrected vertically focused flow. It is important to note that the movement of the fluid in the analysis channel is not just simply up or down but also outward. The fluid is stretched and shifted at the same time but the net average effect on the sample sheath is a downward flattening.

By running a simulation backward in time for this tuned flow configuration, it is possible to see what a perfectly focused flow would require. Starting with a line of traces past the subtraction junction, near the analysis channel outlet, the simulation was run in reverse. Traces ran upstream of the junction and the result showed that a gull wing-like profile entering the subtraction junction would result in the horizontal profile afterward. Based on the results of the previous sections, this type of profile can be created by adding three sheath layers together at different flow rates.

In contrast to that, if an addition junction itself were the final step it would produce a gull wing profile so to correct it, the incoming profile , it would require an inverted gull wing-like profile which could not be achieved without a large number of

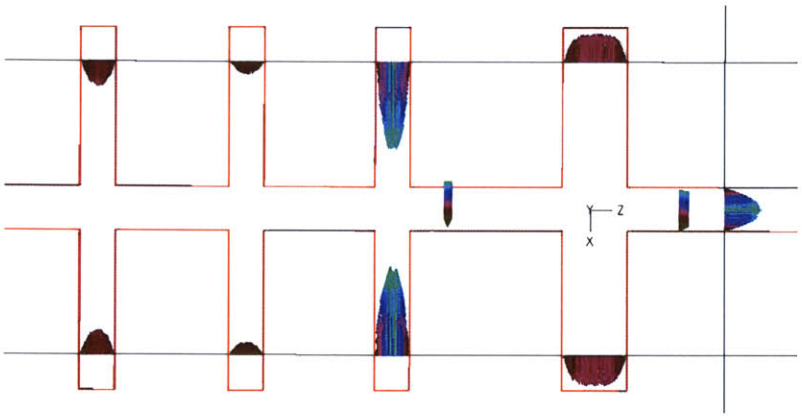

Figure 2-15: Tuned flow. Three sheath channels to the left introduce flow and the wider channel on the right removes flow. The bulk motion of the fluid in the analysis channel is still downstream along the z-axis. Two lines of trace markers used to trace the flow upstream and downstream through the 4th junction.

additions and subtractions before it. The fact that for a two-level design channels on a chip cannot cross each other without some type of fluid exchange eliminates this as a practical possibility.

2.5 Mask Design

Using the results of CFD modeling, a multi-channel chip was designed to test the flow tuning hypothesis and overall effectiveness of reducing the depth of field of the sample sheath.

Physical dimensions of the chip were determined by a few key features:

1. The ability to fit on a standard microscope stage - The standard 96-well plate used in biology measures no more than 5 x 3.5 x 1 inches.

2. The inlet wells be spaced to match dimensions of multi-tip pippetters commonly used in automation or other high-throughput liquid handling.

3. The width of the chip could be no more than 2.5 inches in order to fit into fixtures used during fabrication.

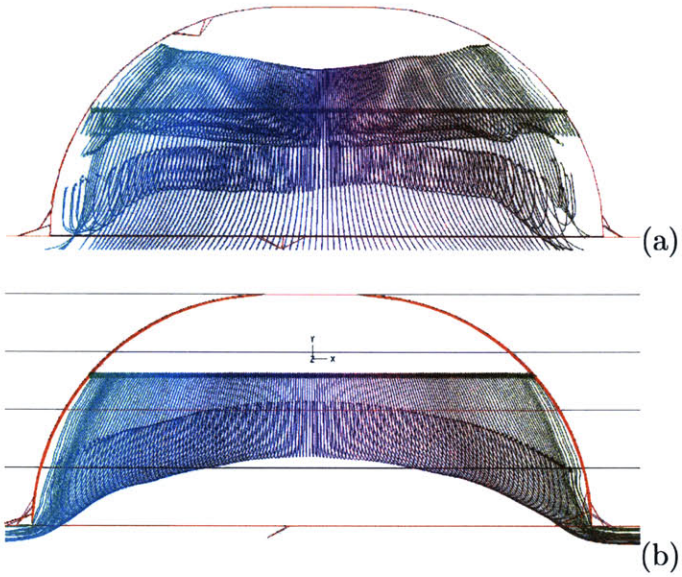

Figure 2-16: Subtraction junction of line width 150-micron and etch depth 100-micron. (a) Markers placed downstream of the junction and then traced upstream. The uppermost profile is just before the junction and the lower, more complicated ones are upstream beyond the addition junctions. (b) Markers placed upstream of the junction and then traced downstream through to the exit of the analysis channel.

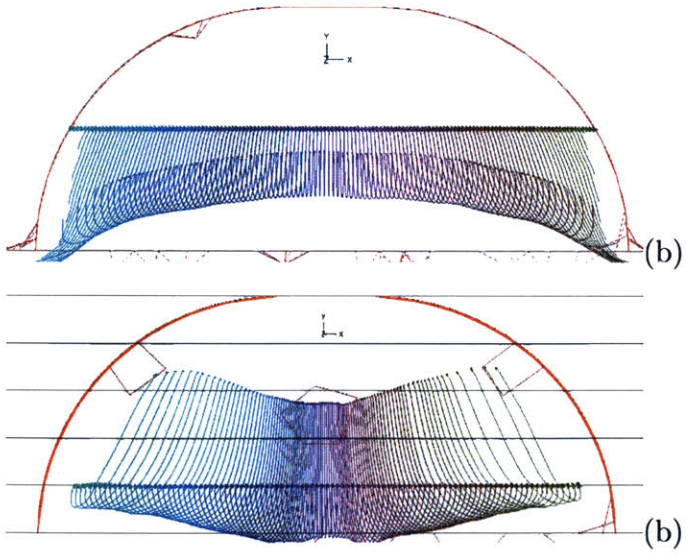

Figure 2-17: Addition junction of line width 40-micron and etch depth 100-micron. (a) Markers placed downstream of the junction and then traced upstream. The resulting profile is similar to that of the previous figure except less pronounced. (b) Markers placed upstream of the junction and then traced downstream through to the exit of the analysis channel.

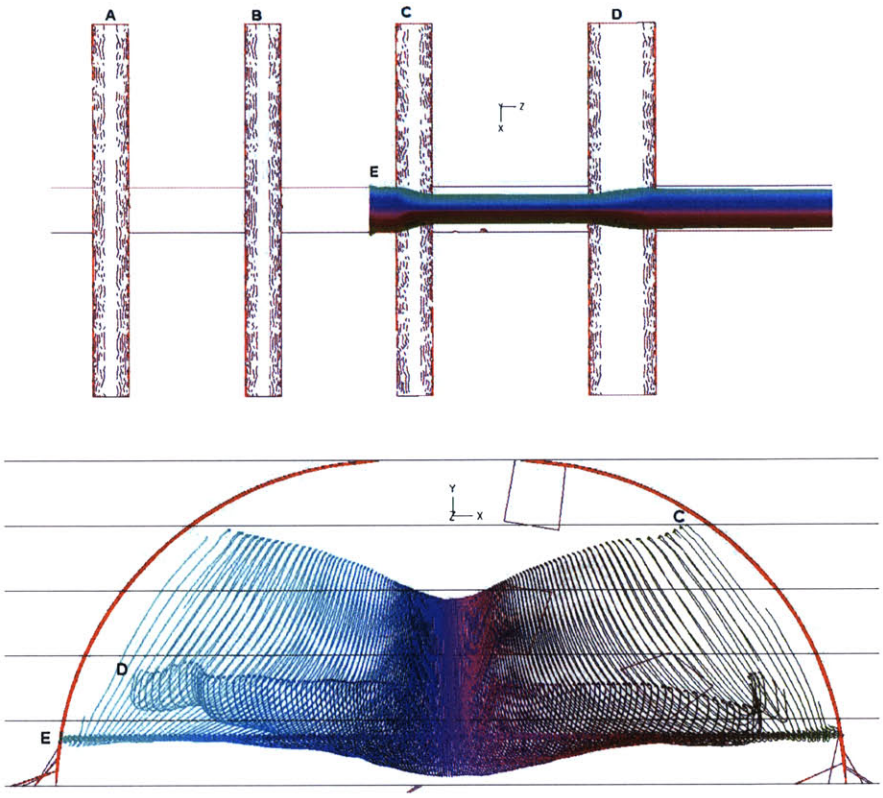

Figure 2-18: Trace (E) placed after Junction 2 (B) 15 microns above the bottom of the channel to mark Sheath 2 flow. As it passes through Junction 3 (C) it is focused upward and inward into a gull wing profile. As the traces pass through Junction 4 (D) they are preferentially pulled downward and outward. The relatively flat layer of traces that is formed is approximately 20 microns higher than where the original traces were placed.

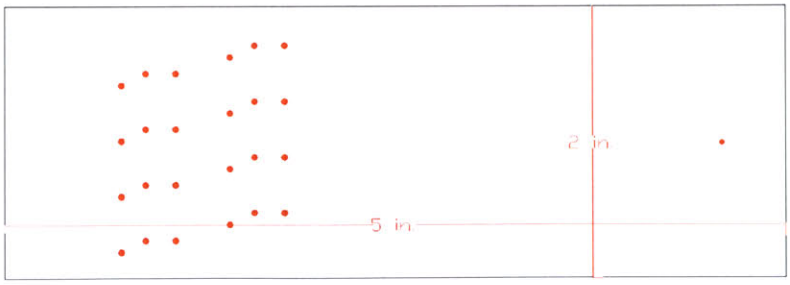

Figure 2-19: Pattern for inlet channels on the left hand side. Single port outlet on the right hand side. Focusing, tuning and scan regions in between.

To produce the flow profiles created in the CFD software along with other variations, channel length was chosen over line width or etch depth to control the flow rates of each of the sheath layers. In general, wet etching involves a large amount of experimental calibration and is a difficult parameter to control; therefore, it is much easier to maintain precision through mask printing which is a commercial service with published standards for quality and resolution. Even with less stringent mask printing, any small variations that were present in the mask would be smoothed out by the more dominant etching process so long as the photoresist was not underexposed. The use of length to control resistance led to sometimes long and densely packed areas of serpentine channels. If more resistance was need, more turns were added. If less resistance was required, a single lane was split into parallel lanes at a y-junction and then brought back together later on. Line width was never decreased or increased. This concept runs exactly parallel with building a resistor network with only one resistor value. Varying line width would have created more compact patterns but then the relative resistances of each sheath channel would have been dependent on the etch depth [5]. In the serpentine regions, the line-to-line spacing was only 400 microns. Leaving at least a quarter of the glass surface in tact for bonding, the maximum etch depth was 130 microns. Given the amount of space to work with between the inlet pattern and the outlet port, 8 parallel analysis channels were laid out with a minimum and maximum sample sheath of 10% and 33% and a maximum subtractive flow of 50%. Table 2.1 shows the specific ratios of each of the eight channels.

This set of flow ratios was selected to test the various parameters of vertical hydrodynamic focusing. Between Sheath 2 and Sheath 3, flow would be introduced in multiple values in the range from 25 to 70%. Flow would be subtracted from the analysis channel at values between 17 and 50%. Correction channel line width would also be varied from 120 to 200.

The choice of when and where to use etch depth or line width to control profiles was influenced by the fact that each original glass plate (one half of the chip) can only

[5]Resistance for internal pipe flow was calculated using an equivalent diameter for a non-circular cross section, $D = 4 \times (area)/(perimeter)$, also known as the hydraulic diameter.

Channel	Sheath 1	Sheath 2	Sheath 3	Correction	Final
A	33	33	33	17	40/40/20
B	11	11	78	25	15/15/70
C	25	25	50	30	36/36/29
D	15	15	70	50	30/30/40
E	20	20	60	25*	27/27/47
F	10	30	60	25*	40/13/47
G	30	10	60	25*	40/13/47
H	20	10	70	17	27/14/59

Table 2.1: Flow ratios for each of the 8 lanes.
* line widths of 120, 160, 200

be etched to only one depth. This meant that line width would have to be used to create a difference in profile between the sheath layers and the correction layer. The line width of the correction junction was increased to 150 microns. A self consistent scheme of controlling the amount of correction was used. The correction channel was routed back to the analysis channel slightly further downstream. Between the point of correction and the point of reintroduction of the correction fluid, the pressure drop was exactly the same. This being the case, the ratio of correction fluid drawn could be precisely controlled, once again, by the length of the correction channel. This was better than connecting directly to the outlet port because it required less channel length which reduced the chance for variations in depth and width of the channel.

Overall, this design was kept as simple as possible to test the idea of flow tuning. A minimum of 3 junctions was required for the three sheaths of hydrodynamic focusing. In this design each sheath layer requires an individual well to maintain separate fluid solutions. All flow is driven by a single port at the outlet and layering is controlled by relative resistance of the sheath channels. Only one additional junction is used for further tuning of the flow. Each lane operates independently so lanes will maintain the same focusing profile for a large range of flow velocities. Most of the channel layout is located away from the optical window. Other features of the mask design included visual alignment marks which are also used as test regions for a surface profilometer during fabrication and additional lines to connect any isolated features so that water and air could escape during bonding. The intended mode of operation

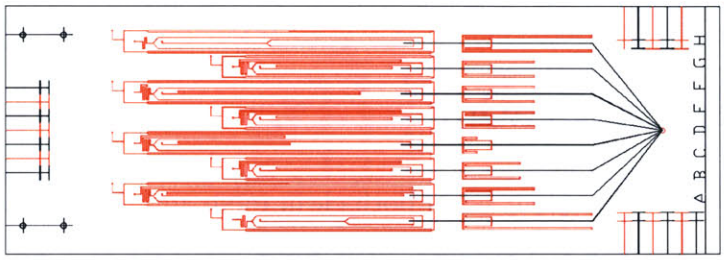

Figure 2-20: Eight-lane pattern. Black and red denote top and bottom halves of the chip. 24 inlet wells. One outlet port.

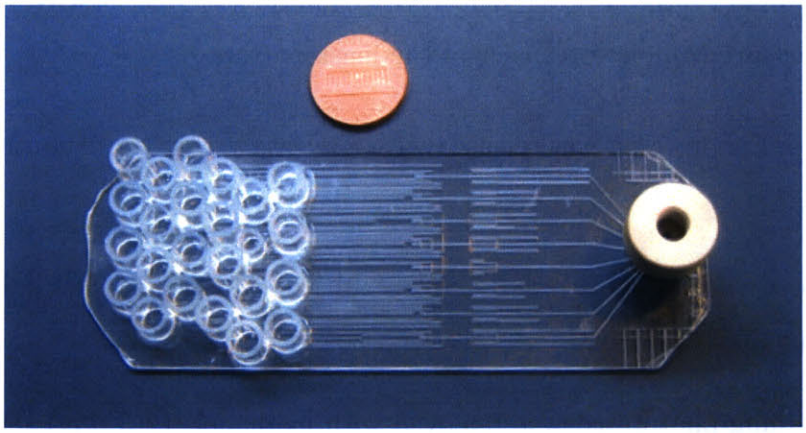

Figure 2-21: A fabricated chip using the mask patter shown in Figure 2-20.

is with the flat side of the analysis layer facing whatever optics are scanning it, i.e. if the analysis later is on top, the microscope objective should be below the chip looking up.

A CAD file of the mask design created in AutoCAD2000 was sent to a commercial printer[6] and a face down negative emulsion mask was printed.

2.6 Chip Fabrication

Fabrication of the chips occurred in both clean room and normal biological lab space clean enough for cell and DNA work. The times listed for each process are approximate because photoresist can change from batch to batch and the etchants and release agents are reused several times before disposal. Based on the conclusions from the simulations, the target etch depths for each chip was 75/100, 100/100, and 100/125 microns.

1. The photoresist was put in contact with the mask and exposed to UV light . (clean room, 5.5 minutes)

    - As explained in the mask design section, the width of the lines was not as important as the etch depth so the photoresist was slightly overexposed to ensure complete transfer of the mask pattern

2. Exposed photoresist was released with a release agent. (until chrome was visible $\sim$5 min)

3. Exposed chrome mask was released with chrome etch. (until light was visible through glass $\sim$5)

4. Remaining photoresist was removed with methanol. ($\sim$5 min)

5. Glass plates were etched in a buffered hydrofluoric acid bath at room temperature.

[6] Advanced Reproductions

- Three pairs of plates were etched for 80 (sheath) /120 (analysis) , 127/175 and 180/210 minutes at an average rate of 40 microns per hour[7].

6. Remaining chrome was released with chrome etch. (until completely removed ~20 min)

7. Inlet and outlet port patterns were laser drilled

8. Organic matter was cleaned off with a sulfuric acid bath. (overnight)

9. Inorganic matter was cleaned off with an ammonium hydroxide bath. (overnight)

10. Particulates washed off with ultra-pure water. (clean room, 1 hour)

11. Soft bonding - two halves were wetted and brought into contact and aligned. Water was removed in a low temperature oven. (clean room, ~8 hours)

12. Hard bonding - soft bonded chip were thermally annealed to near the glass transition temperature to permanently fuse the two halves. (~24hours)

13. Bonded plates were diamond cut into individual chips.

14. Wells and fixtures were attached to chip with epoxy and cured.

[7]Two of the three pairs of chips were inadvertently over-etched. Surface profilometer measurements taken at 30-minute intervals indicated that the etch rate was slowing down so initial etch times were increased. Later inspection under a microscope revealed that the measurements had been inaccurate. The real etch rate of 40 microns per hour was determined post-etch. Maintaining a sufficient intact-to-etched surface ratio also played a role in bad etch quality. As the glass was etched away, the chrome mask was left to hang over the empty space. The removal of too much glass combined with movement of the etching solution over these regions of the plate caused parts of the mask to peel off.

Chapter 3

Experimental Results

Experimental tests were organized in a fashion to analyze three main properties of the vertical hydrodynamic focusing: two-fluid flow profiles, three-fluid focusing of a sample fluid, and vertical correction of focused flow. Additionally, it was also a chance to see the practicality and ease-of-use of the design.

3.1 Setup

The Zeiss LSM 510 was selected to characterize the flow in our chip after attempts on the PerkinElmer were unsuccessful even with image processing. A 10x objective was used because of the large working distance needed. All other objectives had working distances less than the 0.7-mm thickness of the glass used for the chip. Even with the lowest magnification available, it was still possible to take 1024x1024 pixel images (0.9 microns/pixel) with y slices of height 5.6 microns at intervals of 2.8 microns. Three dimensional images were created and measured using the Zeiss LSM Image Browser[1].

Earlier issues of bead tracking resolution were overcome by using a 5 micro-molar solution of fluoresceine and 0.5% solution[2]of 1-micron-diameter fluorescent polystyrene beads (approx. 543/570 nm) and a revised set of microscope settings. The first attempt to characterize the flow involved a high concentration of beads and

[1]version 3.5.0.376

[2]As stated in the Terminology section, concentration is percent volume of the original working solution.

a direct cross section of the stacked 3-D image. The high concentrations resulted in high fluorescent intensities which the microscope could not resolve very well when coupled with the motion of the beads. The high concentration of beads also led to a build up of beads on the channel walls which was very difficult to remove. At lower concentrations, there were insufficient beads to visualize the flow in a single cross sections. Other available built-in options on the LSM 510 were an ability to average multiple stacks or first sum the lines of each slice multiple times and then to create a stacked image out of those slices. These produced better images but raised concerns of contrast with averaging and resolution/noise with summing. In the end, these more time consuming collection methods were not needed. The best results were produced from a once-scanned 3D stack whose gain was minimized to show only the most intense beads. A cross section would reveal almost nothing but a projected image along the axis of flow produced a very well defined profile. This was essentially a post-collection summing of the image that was valid because the imaging window was several channel diameters downstream of the junction. Flow in the imaged channel was fully developed and the residence time of a bead was short enough to ignore diffusive dispersion effects.

A 50% glycerin and water solution was used as the working fluid to help improve image quality. This solution was neutrally buoyant for polystyrene[3] and was not thought to have any adverse affects on imaging or flow. Glycerin is a simple sugar alcohol ($C_3H_5(OH)_3$) commonly used in microscopy to wet lenses so there was no concern with the impact on optical quality or the Newtonian nature of the fluid[4].

The chip used for testing was etched to a target of 75 microns for the sheath channels and 100 microns for the analysis channels. It showed no unbonded regions which would have caused unintentionally connected channels, and there were no noticeable

[3]The exact density of the beads is not known because processing of the beads to give them fluorescence could change the density and is not supplied by manufacturers. A simple test with different density solutions and a centrifuge was used to determine an approximately neutrally buoyant solution.

[4]Optiprep, a neutral density, neutral osmolality solution using an iodine-derived compound, was tested because of its biological inertness but exhibited some sensitivity to flow rate suggesting that it was not a Newtonian fluid. Optiprep is used in the medical industry for imaging but its mechanical properties were not available from the manufacturer.

Microscope	Zeiss LSM 510 laser scanning confocal
Resolution	0.90 μm z-x, 5.6 μm y
Filter Sets	FITC (488/515), Rhodamine (543/570)
Chip Lanes	8 parallel lanes
Flow Rates	100, 200, 400 μL/hr/ (approx. 175, 350, 700 microns/s)
Working Fluid	50% glycerin in water (dynamic viscosity[4] - μ =6.00 cP, density - $\rho = 1.13\times10^3$ kg/m^3)
Dye	5μM fluoresceine
Beads	0.5% 1 μm polystyrene (emits strongly in red, 580 nm, and weakly in green, 520 nm)

Table 3.1: Setup specifications

variations in channel width. Only partial data was obtained from Lane F because the inlet ports were accidentally sealed with epoxy while reattaching a well. Some data for other lanes was inconclusive because of irregularity in flow from trapped bubbles or debris.

3.2 Initial Observations

During the initial setup many observations were made about a range of issues that would possibly have an affect on the imaging results and the ability to directly compare them with the simulated conditions. Some were related to fabrication, others on design and a few on the experimental setup.

The first and most noticeable concern was the geometry of the channels. A non-confocal top-down view of the channel revealed some error in etch depths compared to the 75 (sheath) and 100 (analysis) design targets. The actual values in the device were approximately 60 (sheath) and 105 (analysis) microns[5]. This was unexpected considering that both halves of the chip had been etched in the same bath at the same time except that the analysis half had been left in the bath for 50% longer. Subsequent confocal images showed that the depth of sheath channels were approximately 55 microns and the analysis channels were approximately 75 microns (Figure 3-1). This

[5]Approximate etch depth calculated from line widths using an ideal line width of 40 microns and observed channel widths of 160 and 250 microns

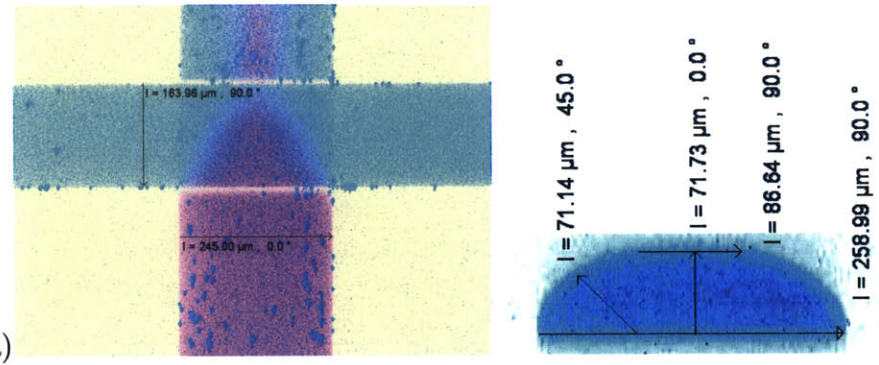

(a) (b)

Figure 3-1: Top Down view and cross section of a junction. (a) The vertical channel is the analysis channel and the horizontal channels is the analysis channel. (b) An image stack showing the full geometry of the cross section.

showed that the etch rate was close to expected but that the actual geometries of the channels had still deviated substantially from the ideal isotropic etching assumed in the models. This was most likely due to edge effects in channels even though the chrome mask remained intact. Additionally, taking measurements at various points along a single channel showed variations in total width of up to 30 microns. The sheath channels of each lane span approximately the same distance so that this variation should affect all channels equally but nonetheless, this was another deviation from ideal conditions.

The sheath channels were all subjected to the same etch bath so they maintained approximately the same relative flow rates. Of much greater concern was the correction junction of each lane. These had been designed for a range for 17 to 50% correction but this seemingly small change in geometry resulted in a 5x increase in the resistance of the correction channels relative to the analysis channels[6]. The maximum correction achievable in this chip was, therefore, Lower than intended. Imaging of Lane D with a designed 50% correction but operating closer to 10% showed no noticeable change, much less correction, in the flow (Figure 3-2). The solution was to "short circuit" the correction channel of each lane with a small modification. A small diamond coated drill bit (approx 1 mm) could be used to drill a hole to join adjacent bends of a channel without damaging the analysis channel or neighbor lanes. Some

[6]Approximate resistance based on a hydraulic diameter.

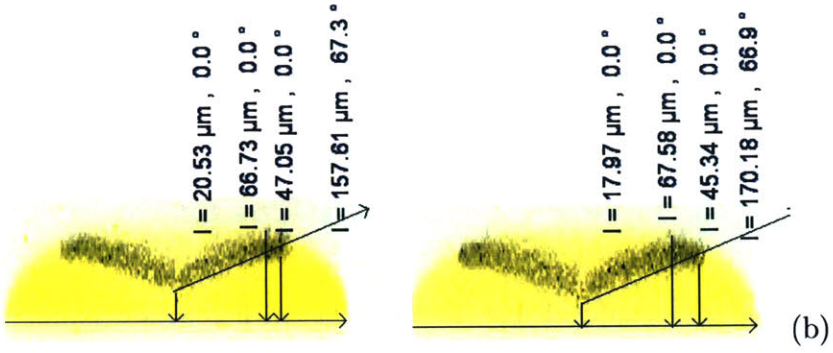

Figure 3-2: Junctions 3 (a) and 4 (b) of Lane D. The fabricated chip was such that even in Lane D, the lane with the most correction, there was no noticeable change in the flow profile.

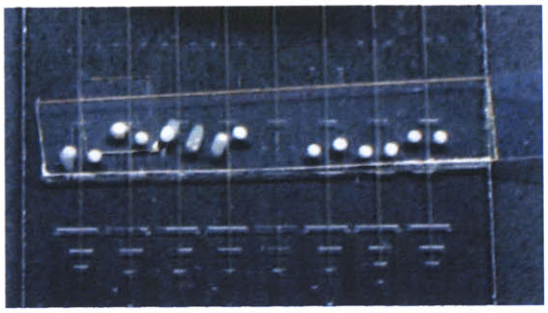

Figure 3-3: One millimeter holes drilled into the correction channels to provide greater correction at approximately 30%.

channels were sealed by the glass debris from the drilling but the newly short-circuited channels (Figure 3-3) were expected to correct at approximately 30%.

Another concern was the accumulation of beads. High concentrations of beads (2% or greater) had a tendency to accumulate around sharp corners or edges at the junctions (Figure 3-4). These accumulations of beads could sometimes become large enough to have an affect on the paths of beads flowing close to the walls of the channel. Also, clumps of stationary beads in the imaging window overpowered the intensity flowing beads so that image quality was reduced. The only way found to remove these beads was to repeatedly push and pull milliliters of fluid through the chip. One positive effect of the stationary beads was their use as a reference for resolution. Individual beads attached to the walls could be simultaneously imaged with flowing beads. These attached beads were sometimes imaged in 3 or 4 slices

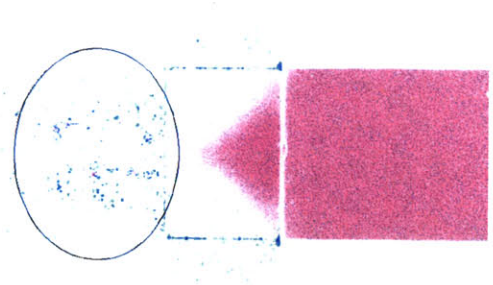

Figure 3-4: A single confocal slice at a junction with analysis channel flow going left. Light debris build-up (circled) can be seen shortly after the junction.

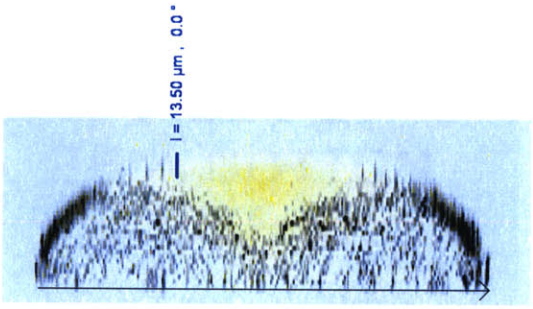

Figure 3-5: Bead resolution. A length marker was placed beside a blurred image of a stationary 1-micron bead showing approximate vertical resolution of 4 slices or 11 microns.

(up to 11 microns) in a given stack (Figure3-5) showing that the bead resolution was somewhat worse than the microscope's slice increment.

Another problem was one that is shared by all microfluidics - bubbles. Bubbles in the channels could sometimes be forcefully pulled or pushed out but pushing fluid during testing contaminates the various wells. It was more useful to eliminate as much of the trapped air as possible before filling the wells with specific solutions. This was done by passing the entire chip under flowing hot water while pulling fluid at the same time. The expanded air was more easily pulled out, and once the chip cooled any remaining air usually settled into the dead space at the very beginning of the analysis channel where it had no detrimental effect. The wells were then filled with working solutions and then pulled by the syringe pump until the chip reached steady state concentrations. Occasionally, small bubbles would become trapped in the junction itself. These bubbles were not large enough to block fluid flow but too

large to freely flow through the channel. When this happened during testing, we could not find to force the bubble out. This was the case for Lane B during one imaging session and Lane D another time. The result is altered relative flow rates and also changed flow profiles from the fluid flowing around the bubble at the junction. Also note that Sheath 1 of Lane H was accidentally contaminated with a low concentration of beads so that Sheath and Sheath 2 were not as easily distinguishable.

3.3 Flow Tuning

Imaging of Lane H showed a two-layer flow with a geometry that resembled the ADINA simulations. When Sheath 3 was added to that flow, the three-layer flow with the vertically focused sample layer had the expected gull wing profile, and images of the focused flow taken after the correction junction also showed a flattening effect on the gull wing profile (Figure 3.2). In addition to the observed change in the shape of the profile, measurements showed an increase of 10 degrees in the angle from 60 (measured from vertical) to 70 degrees. The cost of the correction was a downward translation of the sample sheath which brought it very close to the bottom of the channel, i.e. almost no buffer sheath layer below the sample sheath. Additionally, the sample sheath was stretched out so that it covered more of the cross sectional area of the channel after the correction junction.

The correction had worked to flatten the boundary but further analysis showed that the overall depth of field of the sample sheath had not been improved. In Lane H, the Pre-correction sheath spanned 55 microns (15 to 68) in the y-direction, and the post correction sheath spanned 56 microns (7 to 63). If there were any small improvement, it had been lost in the noise of the y-resolution. Lane A showed an improvement in depth of field of 10 microns but this was only a 15% improvement from 62 to 52 microns (Figure 3.3). This, however, did not invalidate the simulation data and the hypothesis of flow tuning and selective correction. Further analysis in the discussion chapter will present models that explain the performance of the chip that was tested and the influence of the actual fabricated geometries and design flaws

Two-layer flow • height at midplane = 0 microns • maximum height = 45 microns	
Three-layer flow • height at midplane = 14 microns • maximum height = 68 microns	
Corrected three-layer flow • height at midplane = 7 microns • maximum height = 63 microns	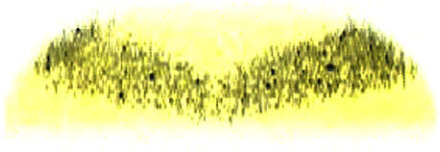

Table 3.2: Flow profile sequence of corrected flow in Lane H.

Two-layer flow • height at midplane = 0 microns • maximum height = 50 microns	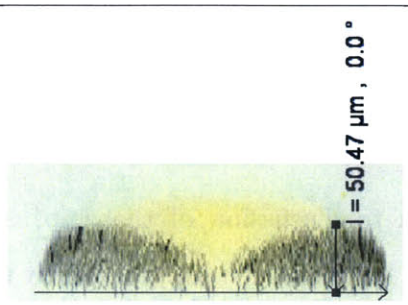
Three-layer flow • height at midplane = 0 microns • maximum height = 62 microns	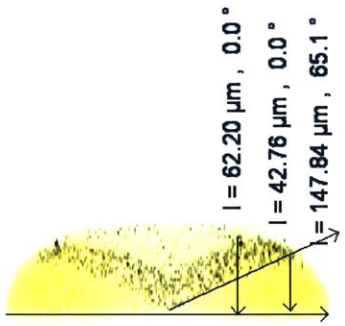
Corrected three-layer flow • height at midplane = 0 microns • maximum height = 52 microns	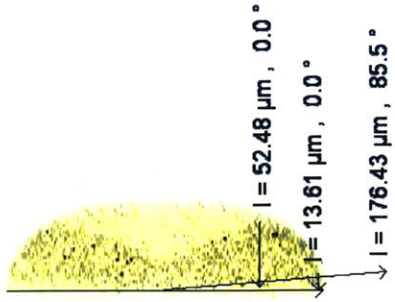

Table 3.3: Flow profile sequence of corrected flow in Lane A.

in its performance.

3.4 Stability, Repeatability and Trends

We now move on to discussion of the chip as a system. Images of the channels showed successful layering over a range of flow rates (100 to 400 μL/hr) (Figure 3.4) but performance of the chip varied noticeably from experiment to experiment. The first two test runs were done at 200 μL/hr on two separate days. A second set of tests at 100 and 400 μL/hr were done in same session on the second day. In general, flows of 100 μL/hr resulted in lower-quality images. Diffusion might have played a small role in this but the variation was most likely mechanical noise. Operating at this speed, one could see (under the microscope) oscillations in the velocity occurring at approximately 0.5 Hz. This was most likely due to the stepper motor in the pump and also movement of the length of unsupported tubing connecting the syringe to the chip. Considering that a 100 micron image stack required 80 seconds to acquire with the selected exposure and resolution settings, this frequency of noise would be acquired by the microscope. Another very likely cause of changes in profile, or image quality, is human error. As shown in Appendix A, 100 μL/hr or 400 μL/hr flow rates did not always result in lower-quality flow profiles and neither did testing at 200 μL/hr on separate days. There was no definite relationship established between total flow rate and image quality so variations were most likely due to changes in experimental setup. Images of the same lane taken one immediately after the other still showed variability in measurement but only on the scale of the vertical resolution of the microscope (Figure 3.5).

Looking at the profiles and the maximum height, one can see that there are variations in different aspects of the profiles but in general Lane G (relative flow rate of 25%) had the smallest height of 45 microns and Lane H (relative flow rate of 75%) had the largest height of 60 microns. The sample sheath layers (Sheath 2) of Lanes A, B, C, D and E were all designed to be introduced at 50% flow rate relative to Sheath 1. Maximum height of the other lanes ranged from 54 to 46 microns. Lanes

	Junction 2	Junction 3	Junction 4
100 μL/hr		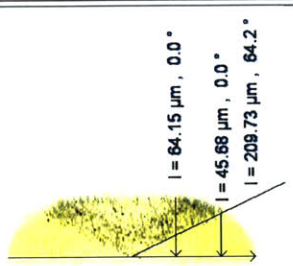	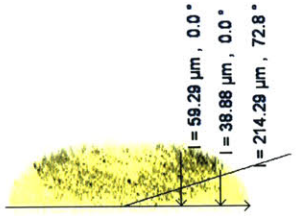
200 μL/hr		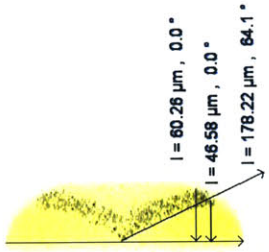	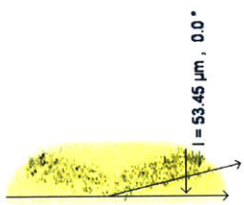
200 μL/hr	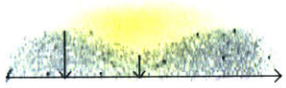		
400 μL/hr		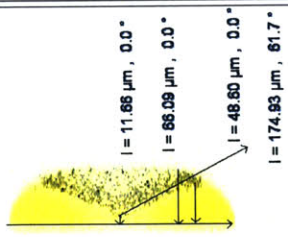	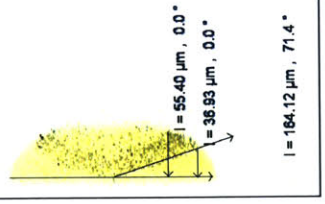

Table 3.4: Flow profiles for Lane H.

	1	2
Lane D, Junction 3	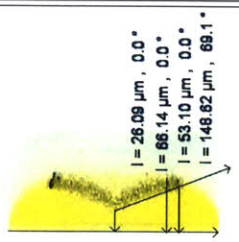	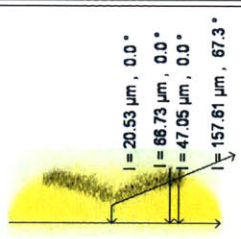
Lane F, Junction 1	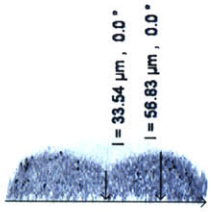	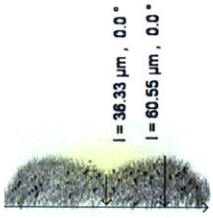

Table 3.5: Consecutive images of the same flow were taken to illustrate the noise in measurement independent of time.

B and C did not appear to close the gap in the middle of the channel while Lane E had a sheath height of 13 microns at the middle of the channel. These variations could have been a consequence of using solely channel length to define flow rate or due to debris that had collected in the channels. Ideally, line length should have been a dependable way to define flow rate but differences in etch conditions across a chip could have led to the variations in the flow profiles. The chip had also been used to calibrate the experimental setup before flow profile data was collected. Although no noticeably large masses had accumulated in the imaging windows, it is possible that this could have been the case elsewhere, especially in the inlet port hole. The chip was baked in an oven at 450 °C to break down all organic material before an initial flush of the channels before use but no additional heat or chemical cleaning was done in between subsequent tests.

Similarly, general trends for other flow characteristics could be established but much of the quantitative values of the data was seemingly drowned out by the noise of the measurements themselves. With a constant ratio of Sheath 1 to Sheath 2 (equal parts of each), increasing flow of Sheath 3 produces a progression of profiles much like what was produced from simulations to compare 60 micron etch depth to 100 micron etch depth. The angle of the wedge becomes steeper as more flow is added.

Lane G 25% Sheath 2 45 micron max. sheath height	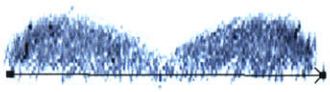
Lane H 33% Sheath 2 44 microns	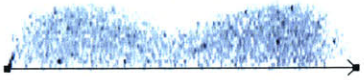
50% Sheath 2 Lane B 50 microns	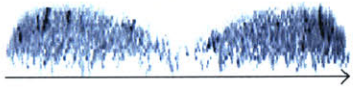
Lane C 45 microns	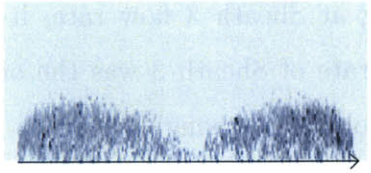
Lane D 47 microns	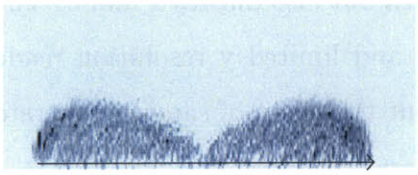
Lane E 46 microns	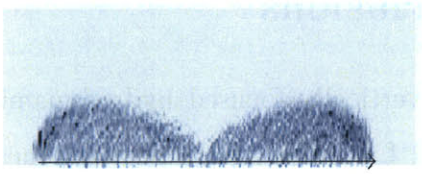
Lane F 75% Sheath 2 60 microns	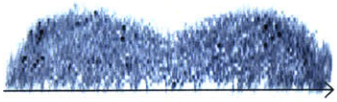

Table 3.6: Two-sheath flow. Increasing percent Sheath 2 from top to bottom.

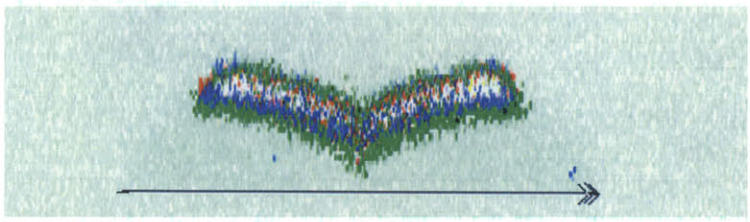

Figure 3-6: Overlaid three-sheath profiles of Lanes F, D and B. This figure is to demonstrate the difficulty of directly comparing profiles in the same manner that was done for ADINA models. The uncertainty in the

The profiles of 2-sheath flow should have exhibited this same trend but the range of ratios was not as high as for 3-sheath flow.

When looking at Sheath 3 flow rate, it was possible to use only certain lanes so that the flow rate of Sheath 3 was the only independent variable. This was not possible when looking at changing sample sheath volumes and the corresponding profiles. The profile of the sample sheath was dictated not only by the flow rate of the sample sheath but also Sheath 1 and 3. The three sheath parameters, a parabolic velocity profile, and limited y resolution made it very difficult to draw any strong conclusions about the effect of sample flow rate on the focused profile.

3.5 Conclusions

In conclusion, vertically focused hydrodynamic flow was achieved and the profiles for Lane H and Lane A support the hypothesized nonlinear flow correction effect; however, vertical hydrodynamic focusing after correction did not show a depth of field improvement over normal vertical hydrodynamic focusing in our device. Even without complete correction, the focused flow could still be a useful tool in that its depth of field is better than the standard horizontal hydrodynamic focusing while having a similar contact area between sample and buffer layers.

If image deconvolution were applied to the analysis process, then the depth of

	400 μL/hr	200 μL/hr
Lane A (33%)	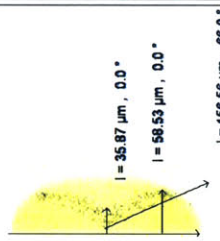	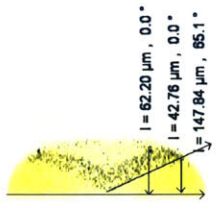
Lane C (50%)	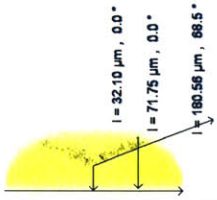	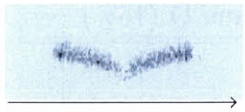
Lane E (60%)	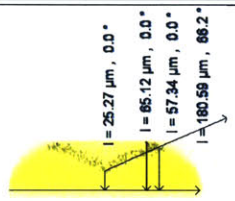	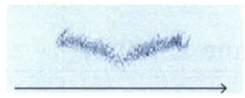
Lane D (70%)	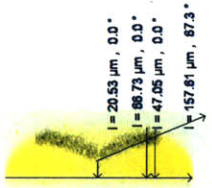	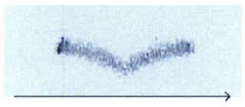
Lane B (78%)	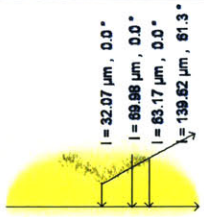	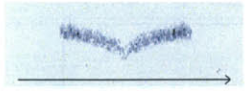

Table 3.7: Three-sheath flow. Increasing percent Sheath 3 from top to bottom. In (400, B) Sheath 1 had a bubble in the junction so that Sheath 3 is likely to be flowing at closer to 90%.

	200 μL/hr	400 μL/hr
Lane G (10%)	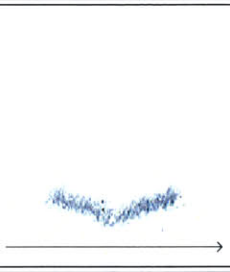	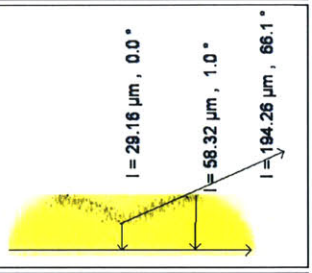
Lane D (15%)	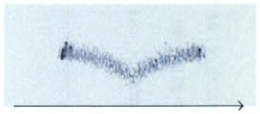	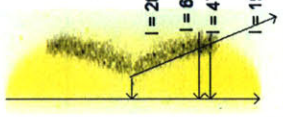
Lane E (20%)	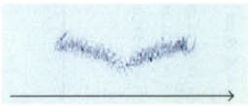	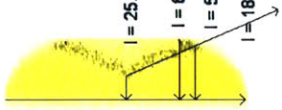
Lane C (25%)	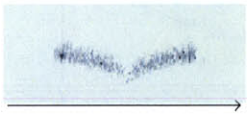	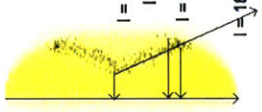
Lane F (30%)	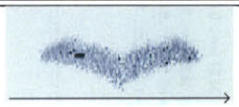	
Lane A (33%)	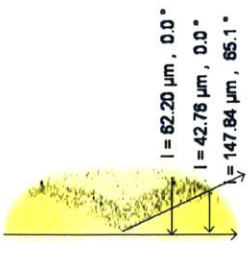	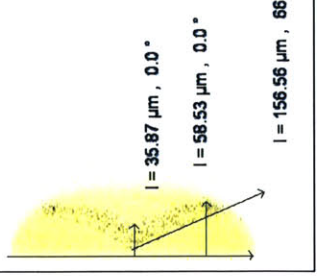

Table 3.8: Three-sheath flow. Increasing percent Sheath 2 from top to bottom.

field requirement for any given target resolution could be expanded to a larger vertical range. The vertically focused sheath demonstrated a well defined thickness and a linear profile after correction which would require simpler algorithms that an unfocused flow.

Much of the focused flow was in the center of the channel where flow is more uniform and shear stress would be smaller on objects such as biological cells. If the overall size of the channel were reduced by a factor of 5, then the depth of field would scale accordingly down to an average 10 microns for the tested designs. The overall flow rate of a system with smaller channels could match that of larger channels if velocity were increased. Because much of the sample sheath is in the low shear stress region and depending on data collection speed, this would not necessarily affect environment of the sample or the performance of the system.

None of this is to say that the test device performed optimally but that it does perform acceptably for many applications.

To improve the performance of the chip, the first area of focus should be tighter tolerances on fabrication. The mask was designed for an aspect ratio of 0.5 (height to width) but was actually closer to 0.30 in the chip. Instead of disturbing the etch process to take a measurement, the plates should be left in for some pre-determined amount of time to give a desired ratio of etch depths based on approximate etch rates . Based on the design of the chip, the relative etch depths of the two halves are more important than the absolute values. That is the beauty of microfluidics and such highly laminar, viscosity-dominated flows. Relative geometry is the dominant factor over a range of fluid properties and velocities.

Even though microscope blurring broadened the sheath layer in the profiles. It was still possible to see that correction was more effective on the bottom half of the profile than the top. This is what caused the profile to stretch in addition to translate. The sample sheath should be focused down to more extreme percentages, 5% or 1%. This is not uncommon in hydrodynamic focusing but the placement of the inlet ports was a big constraint on the design of this chip and how much the sample sheath could be focused. A thinner sample sheath would result in a more uniform correction

throughout the thickness of the sample and also allow for more correction without completely removing the third sheath layer.

Three chips of different depths were fabricated to show the effect that etch-depth ratios would have on the profiles. As shown in the previous chapter and demonstrated by experimental testing, a large amount of flow from a small channel entering into a large channel creates a sharper angle in the introduced flow. This was the profile created by Sheath 3 (clearly seen in Lane B, Junction 3) and corrected at Junction 4 but is not (and was not intended to be) the optimal profile for depth of field improvement. That was what the other two chips were to show. It is unfortunate that only the 50/80 (sheath/analysis) chip was able to be tested because it confirmed flow tuning and correction without actually improving depth of field.

Chapter 4

Discussion and Conclusions

In spite of small but important fabrication variances, the test device demonstrated flow profiles similar to the ADINA models and confirmed the nonlinear dependence on flow rate and channel geometry. New CFD models based on observed channel geometries and some new concepts of analyzing flow profiles will be discussed, and it will be shown that the conclusions drawn from the original models are still valid and that the experimental results do validate and support them.

4.1 Accuracy of CFD Modelling

A new model was constructed based on 80-micron mask line widths and etch depths of 70 microns (analysis) and 55 microns (sheath). The profiles created in these new models correctly predict the images captured in the chip. With the lower aspect ratio, the combined flow rates and geometries of the junctions did not created corrected vertical hydrodynamic focusing. Even for different amounts of correction, the final profile of the sample sheath was still a well define gull-wing profile (Figure 4-1). This shows that the profiles collected in the experiments are correctly predicted by the model and expected for the small fabrication variances. The variations in flow rate and setup contributed to noise in the images but not the general shape of the profiles.

Another observation made during the experimental testing was the dependence of correction on not only x position but also y position. Returning to the CFD models,

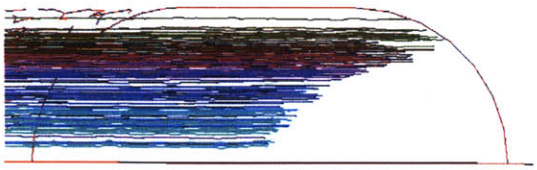

Figure 4-1: ADINA simulation with revised geometry of Lane H based on experimental measurements. A half-profile of flow after passing through the correction junction subtracting 30% of the flow, the approximate value after diamond-drilled short circuits.

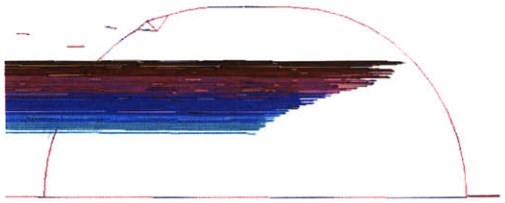

Figure 4-2: ADINA simulation with the designed geometry of Lane H etched to 100 microns corrected 30% in Junction 4. These are the same flow rates shown in Figure 4-1 except with the original intended geometry.

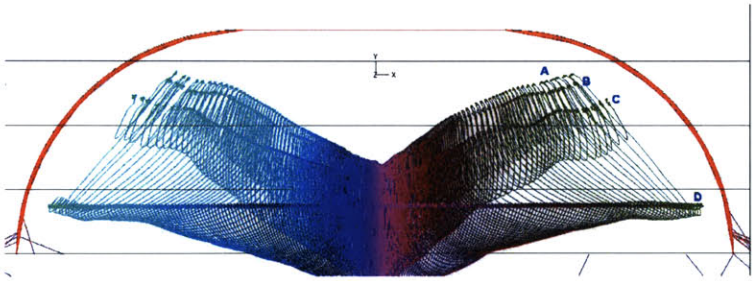

Figure 4-3: X-Y view of Lane H with the fabricated geometry. Tracers placed 15 microns from the bottom before the Sheath 3 junction (d) and allowed to pass through the correction junction. (a) Profile after 70% addition at Junction 3. Profile after correction at two different subtraction percentages: (b) the original 17% and (c) twice the amount at 34%. With this geometry, the effects of correction are minimal and even doubling the amount of correction does little to affect the gull wing profile.

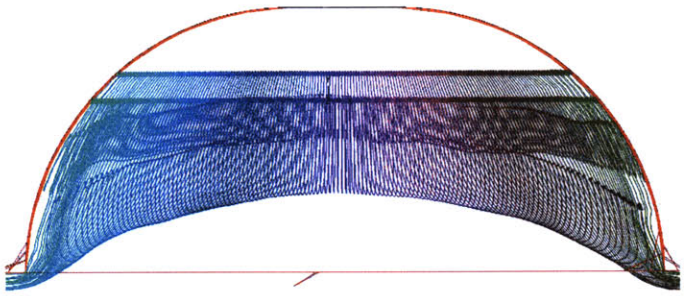

Figure 4-4: Y dependence of flow correction. (a) Horizontal tracers were placed at y = 55 and 65 microns prior to the correction junction. (b) Post-correction, the minimum separation at the middle of the channel has grown to greater than the original 10 microns, demonstrating that correction is also y-dependent.

the trace used to show x dependence can be shifted in the y direction to show that the effects of correction are less pronounced for increasing height in the channel. For two particles along the same horizontal line, the one closer to the edge of the channel will be translated more in the y direction. This was the original observation. The observation that was not made is that for two particles along the same vertical line, the one closer to the bottom will translate more in the y direction. What this means is that if the gull wing profile spans across too much of the height of the channel (the initial depth of field is too great), then the portion of the flow that is closer to the wall but also further away from the bottom will translate the same amount as the flow in the middle of the channel but closer to the bottom. This effect was seen in the fact that the sample sheaths were stretched out and the total range of height before and after correction were the same.

As models grew larger to accommodate more junctions and boundary conditions, particles traces had to travel further for each simulation. Because of this, coarse meshing became more apparent and the two halves (left and right) of the channel began to display different results for particles traveling close to the walls. This was not a major departure from what fine meshing would have created but made it even more difficult to compare the noisy experimental numbers with the results of the models.

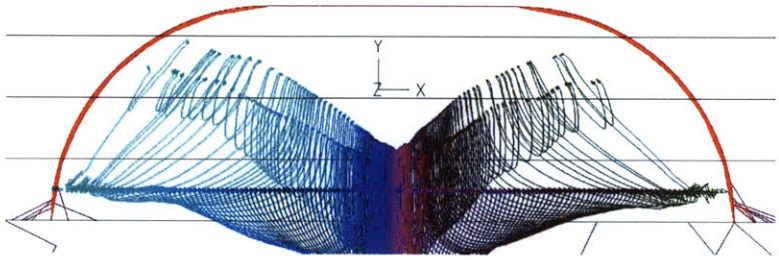

Figure 4-5: Demonstration of nonsymmetric profiles. Horizontal tracers were placed 15 microns from the bottom and allowed to pass through two junctions. At some point, symmetric tracer pairs experience different flow conditions caused by a difference in meshing and that error continued through the life of the trace.

4.2 Chip Design and Future Applications of Flow Tuning

The chip fabricated using the current mask design was able to simultaneously operate 8 different parallel lanes producing vertically focused hydrodynamic flow. Images were collected in a reliable manner and produced sufficient data to show experimental flow tuning and correction and their potential to improve vertical hydrodynamic focusing. When applying this design to a device for actual sample control and imaging one would need to pay strict attention to the etch process and if high resolution is required, use an analysis plate of coverglass-thickness to be compatible with higher magnification objectives.

Flow tuning and correction of vertical hydrodynamic focusing is broadly applicable to microfluidic sample handling. I have demonstrated it as a focusing technique but also that it can be done in a robust material with limited geometries in a simply-operated device. Future devices could be designed for multiples samples in a single imaging window (Figure 4-6), multiple samples with higher focusing ratios (Figure 4-7), or a single sample with higher throughput (Figure 4-8).

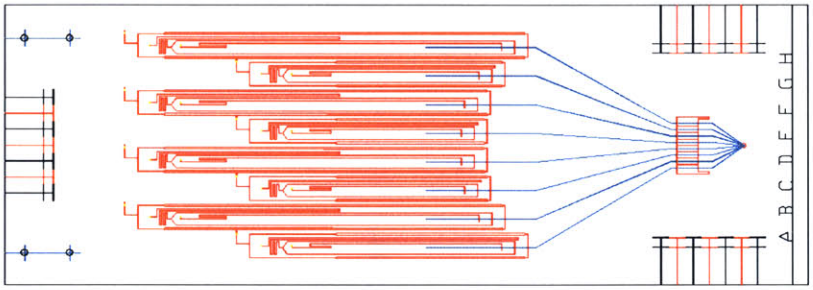

Figure 4-6: Future Design A. Eight lanes with identical flow rates brought to a single imaging window of width 8 mm for easy multi-lane scanning.

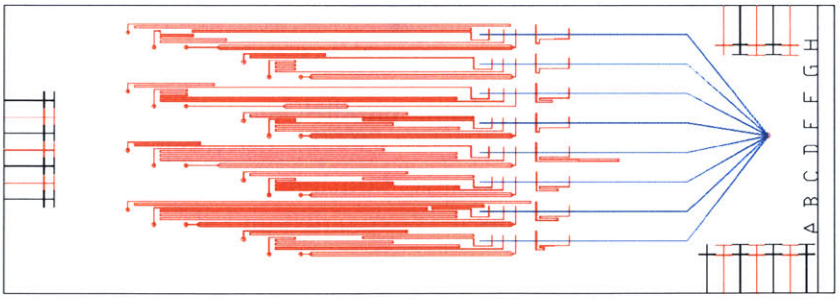

Figure 4-7: Future Design B. The same concepts can be applied to flow focused from a single side of the analysis channel. Symmetry is lost so the profile may be harder to correct but this format allows for a wider range of percentage flow rates of the sheaths.

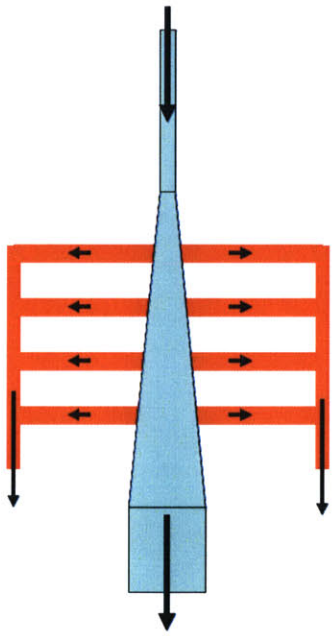

Figure 4-8: Future Design C. If multiple parallel lanes are not necessary, then one larger channel can be designed for a more efficient use of space. Flow can be high-speed before the analysis channel expands. Multiple correction channels progressively correct the vertically focused flow as it is expanded and slowed down.

Appendix A

Experimental Flow Profiles

	Junction 2	Junction 3	Junction 4
100 $\mu L/hr$		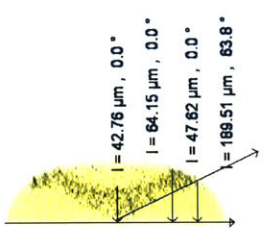	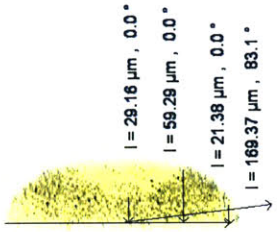
200 $\mu L/hr$		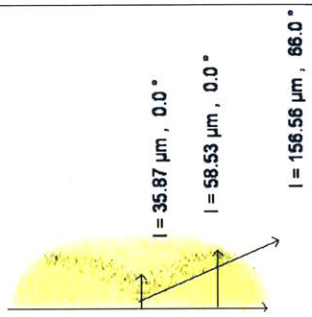	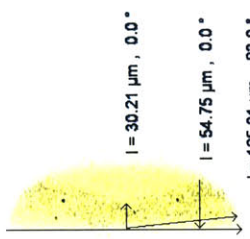
200 $\mu L/hr$	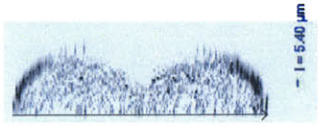		
400 $\mu L/hr$		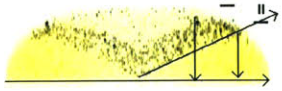	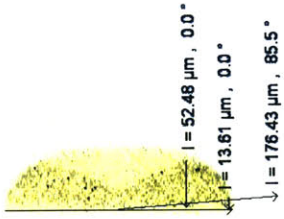

Table A.1: Flow profiles for Lane A.

	Junction 2	Junction 3	Junction 4
100 $\mu L/hr$		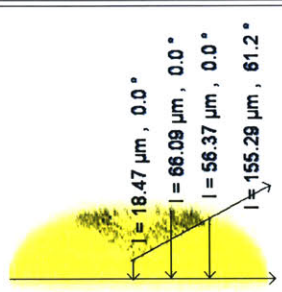	
200 $\mu L/hr$	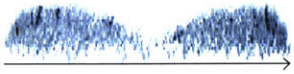	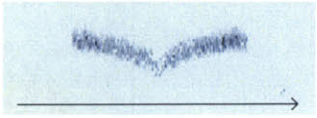	
200 $\mu L/hr$			
400 $\mu L/hr$		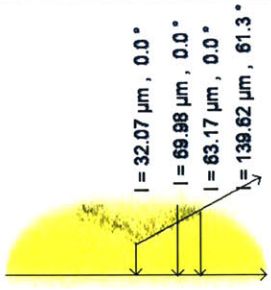	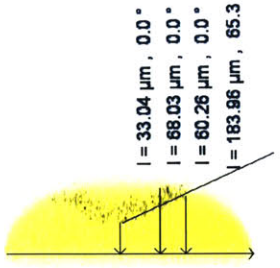

Table A.2: Flow profiles for Lane B.

	Junction 2	Junction 3	Junction 4
100 $\mu L/hr$		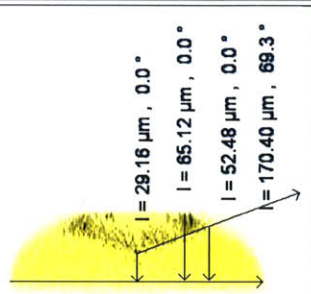	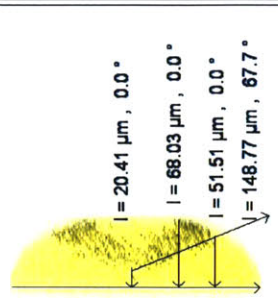
200 $\mu L/hr$		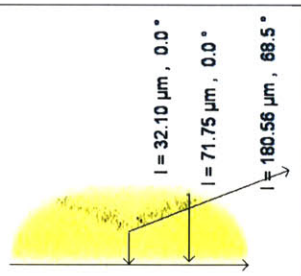	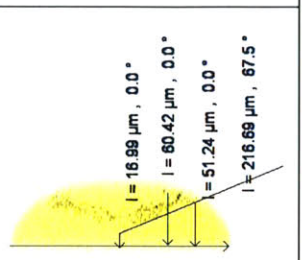
200 $\mu L/hr$	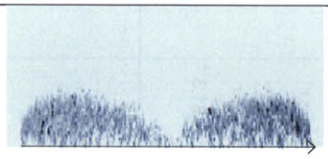	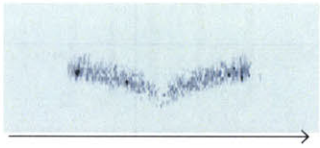	
400 $\mu L/hr$		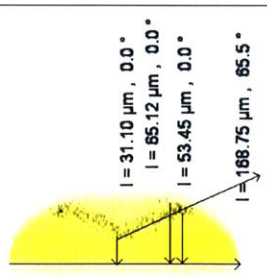	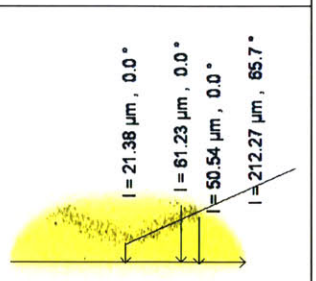

Table A.3: Flow profiles for Lane C.

	Junction 2	Junction 3	Junction 4
100 $\mu L/hr$			
200 $\mu L/hr$		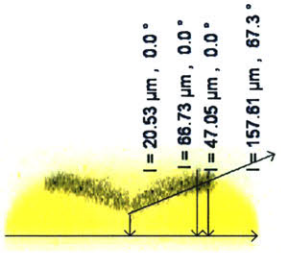	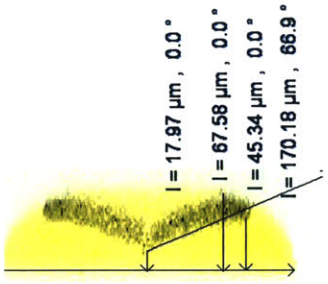
200 $\mu L/hr$	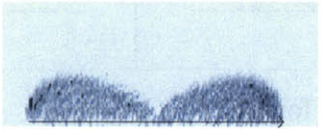	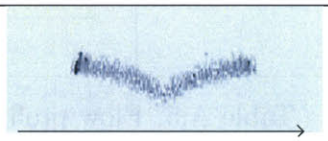	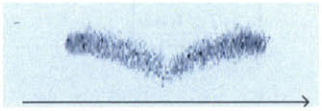
400 $\mu L/hr$			

Table A.4: Flow profiles for Lane D.

	Junction 2	Junction 3	Junction 4
100 $\mu L/hr$		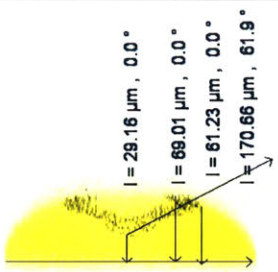	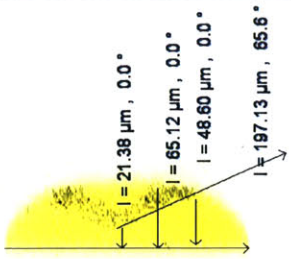
200 $\mu L/hr$			
200 $\mu L/hr$	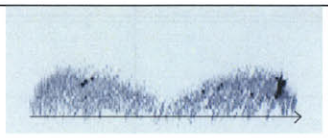	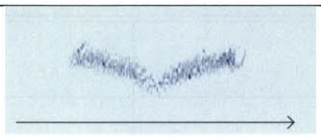	
400 $\mu L/hr$		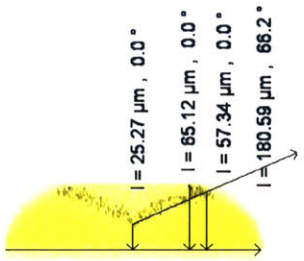	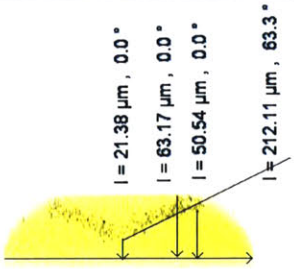

Table A.5: Flow profiles for Lane E.

	Junction 2	Junction 3	Junction 4
100 $\mu L/hr$			
200 $\mu L/hr$	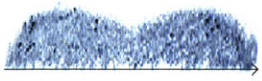	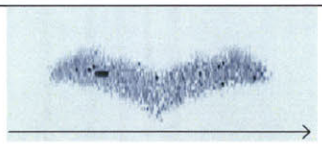	
200 $\mu L/hr$			
400 $\mu L/hr$			

Table A.6: Flow profiles for Lane F.

	Junction 2	Junction 3	Junction 4
100 $\mu L/hr$		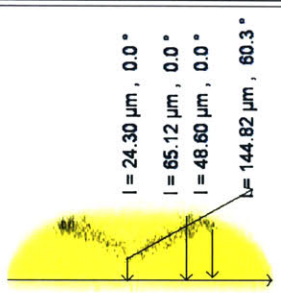	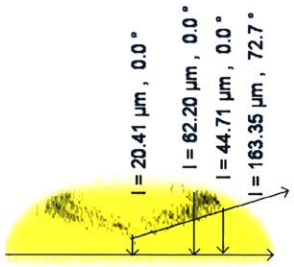
200 $\mu L/hr$	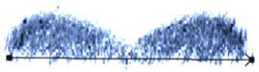	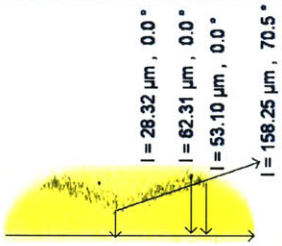	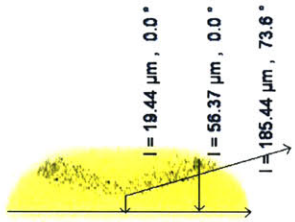
200 $\mu L/hr$		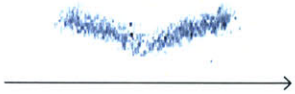	
400 $\mu L/hr$		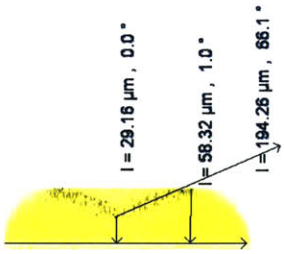	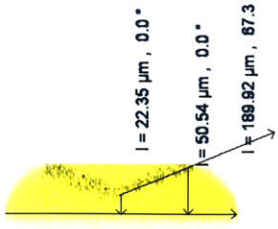

Table A.7: Flow profiles for Lane G.

	Junction 2	Junction 3	Junction 4
100 $\mu L/hr$			
200 $\mu L/hr$	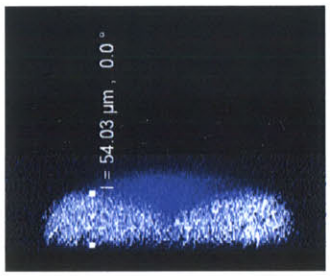	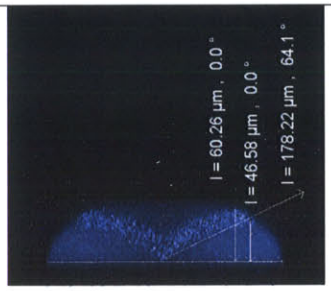	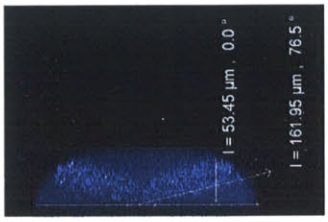
200 $\mu L/hr$		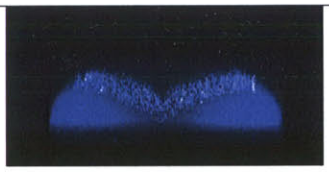	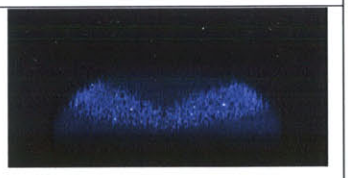
400 $\mu L/hr$		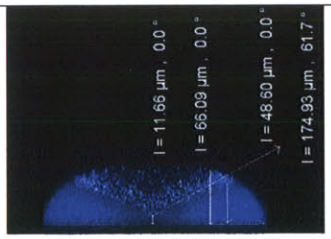	

Table A.8: Flow profiles for Lane H. Shown with negative images to contrast what was shown in the Results section.

Appendix B

Etch Depth-Dependent Simulated Profiles

	10%	30%	50%
20	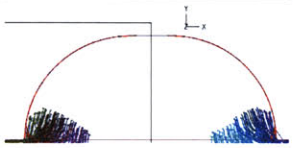		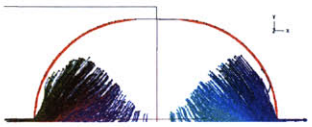
60			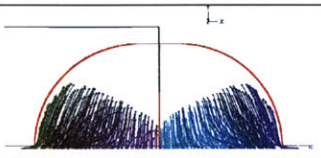
100	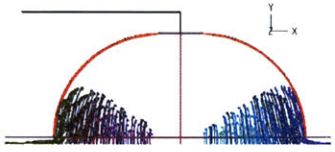	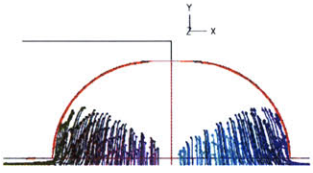	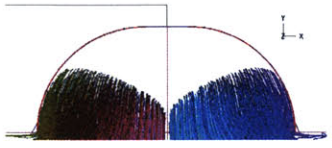
140			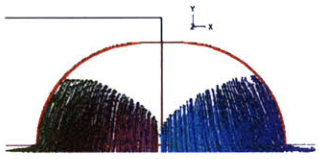
180	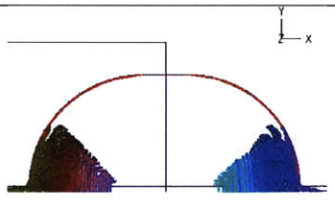		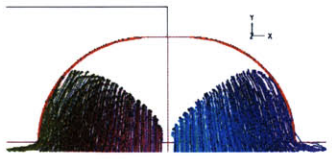

Table B.2: Profiles of flow from varying etch depth and flow rate of Sheath 2.

50%	70%	90%
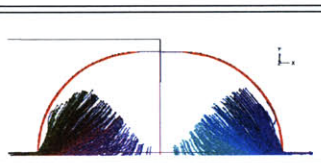		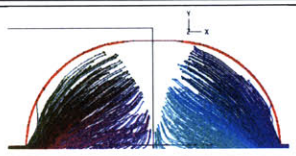
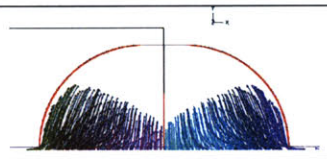		
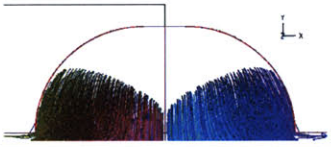	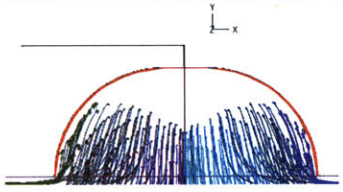	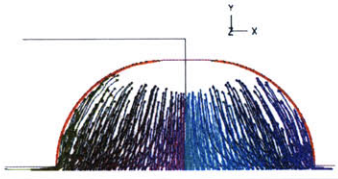
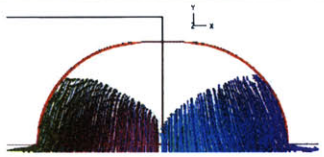		
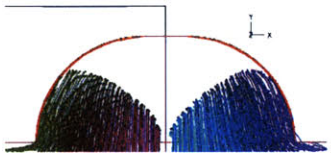		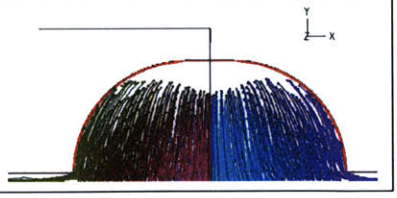

Appendix C

Line Width-Dependent Simulated Profiles

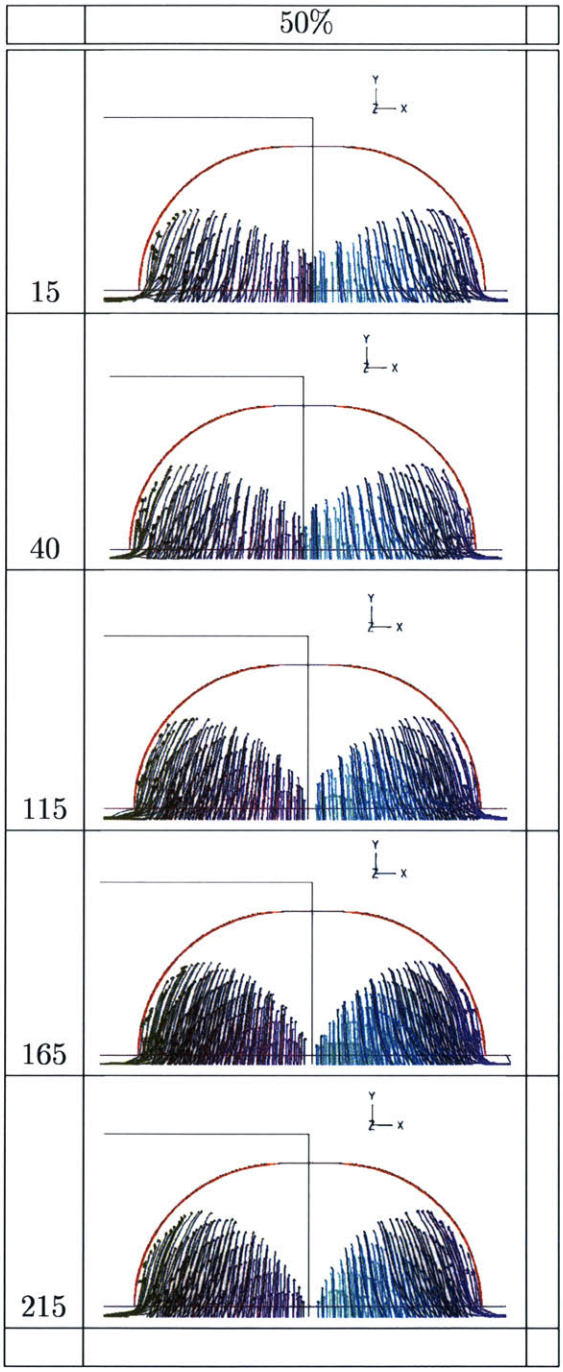

Table C.1: **Profiles of Sheath 2 flow** when varying the line width of Sheath 2 for a constant **50% flow rate**.

Control case for flow rates of 10, 30, 50, 70, 90%

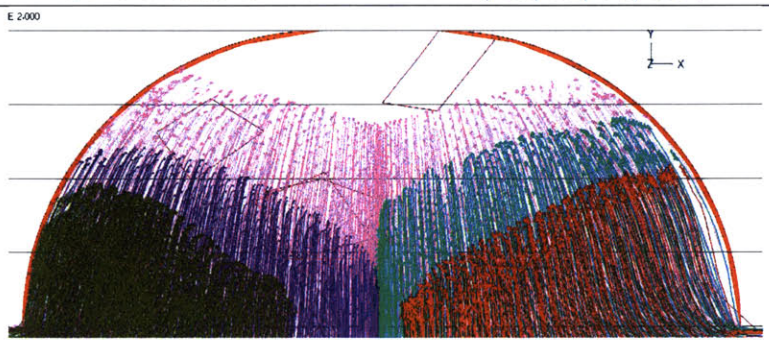

40-micron line vs 165-micron line at 30%

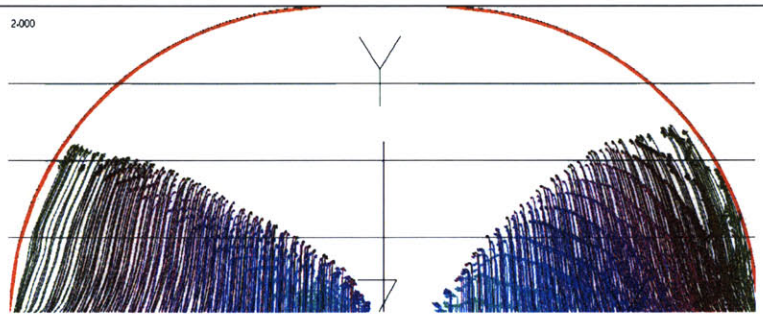

40 165

215-micron line vs 40-micron line at 50%

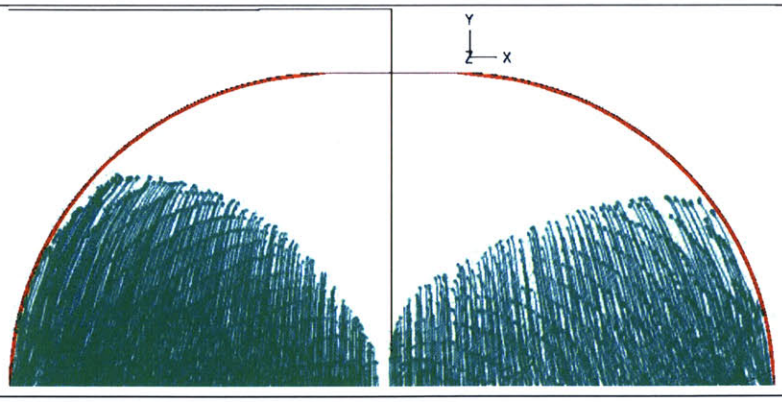

215 40

Appendix D

Simulated 3-Sheath Uncorrected Flows

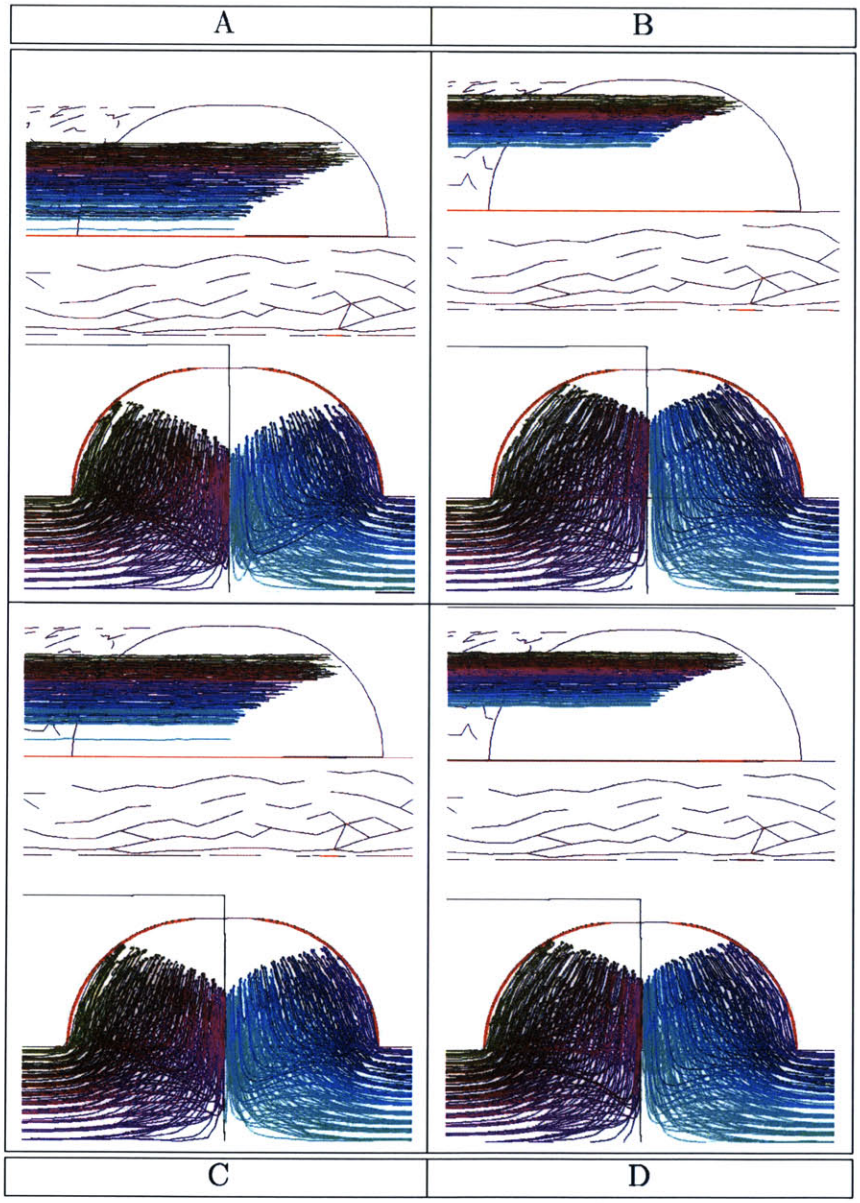

Table D.1: Simulations for uncorrect flows based on lane designs.

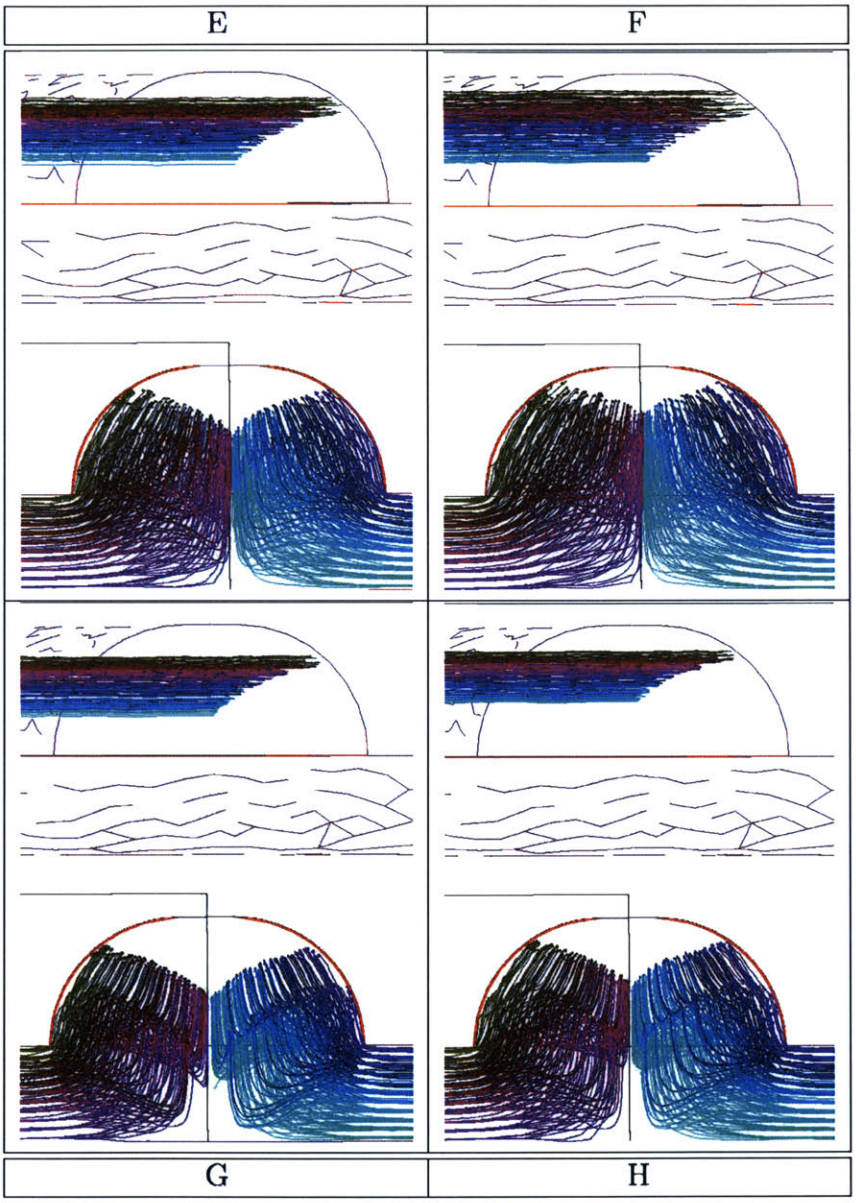
E
F
G
H

Appendix E

Simulated 3-Sheath Corrected Flows

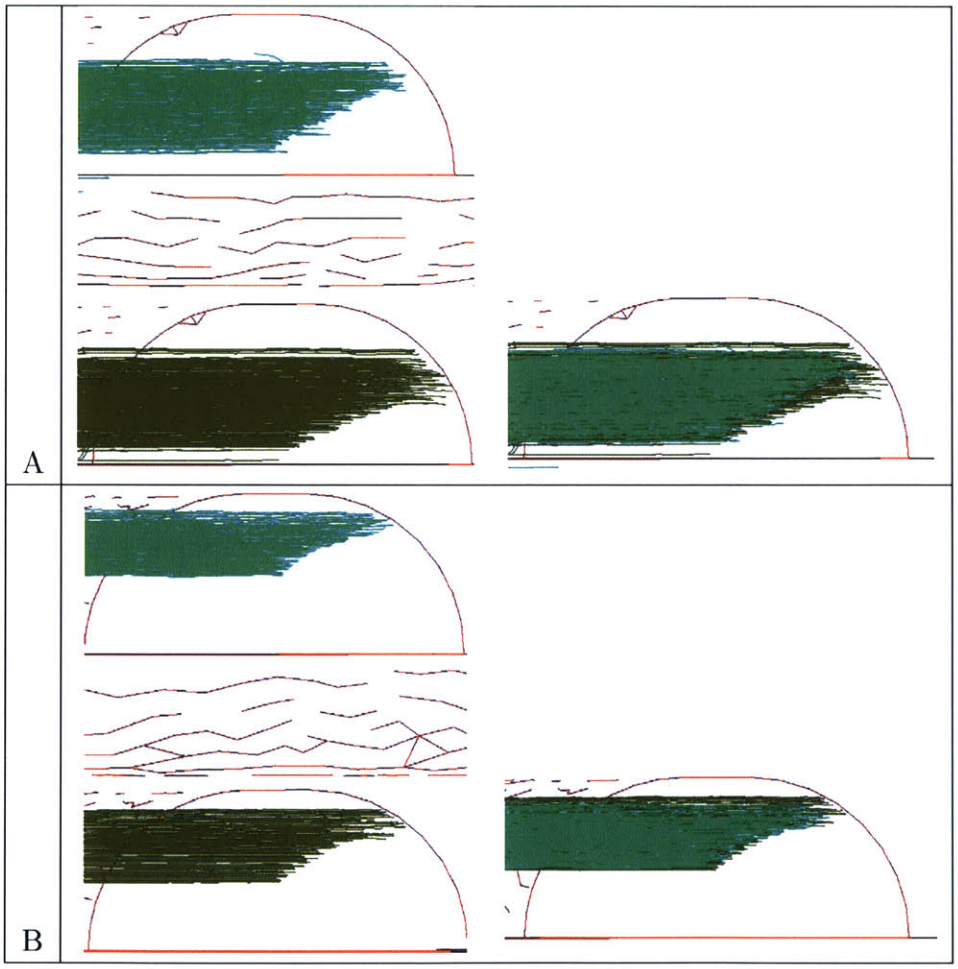

Table E.1: Corrected flow simulations based on lane design. Top left: uncorrected. Bottom left: corrected. Right: overlayed.

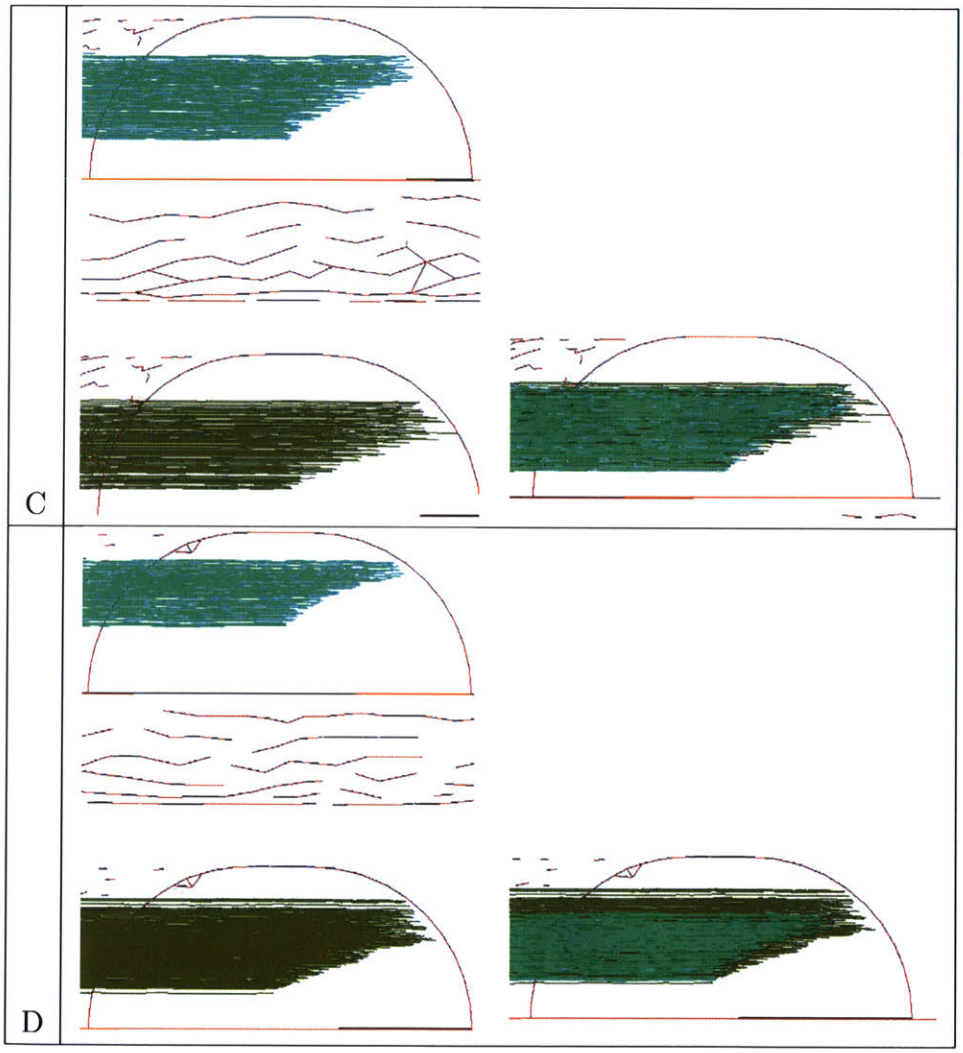
C
D

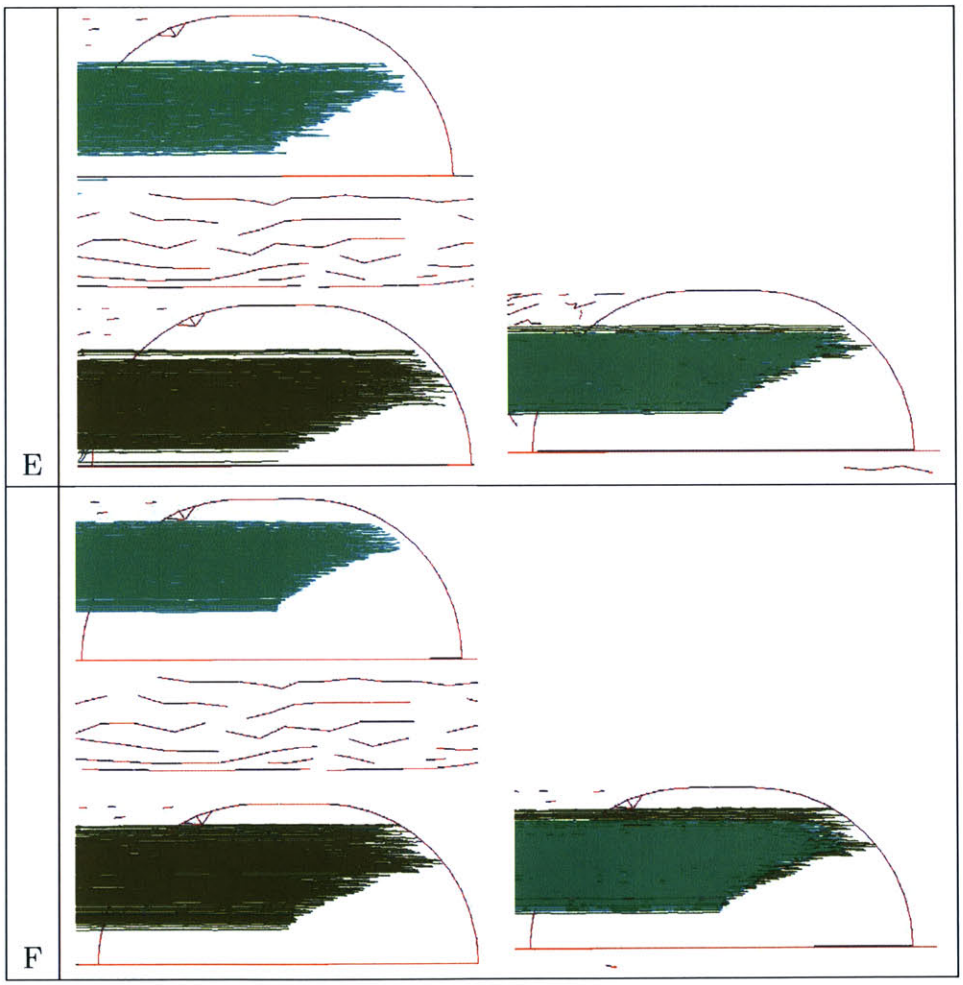
E
F

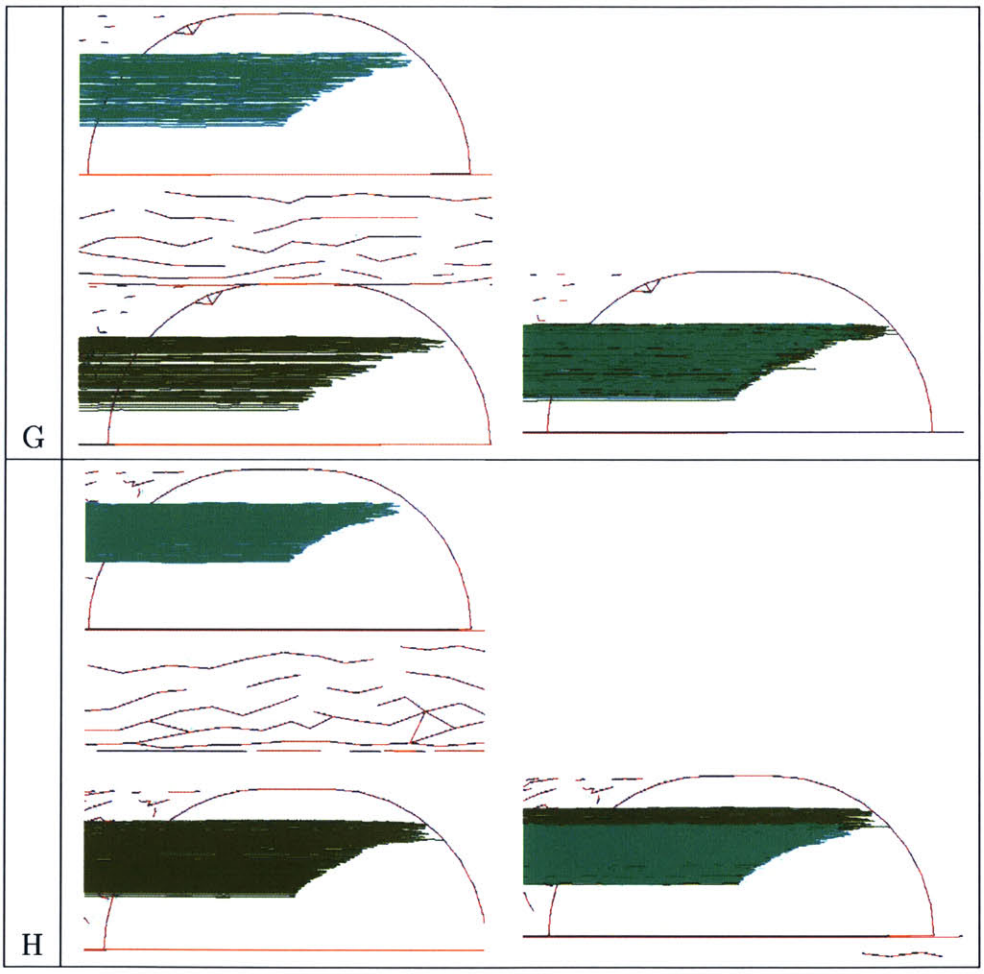
G
H

Appendix F

Sample ADINA Code for Corrected Flow Model

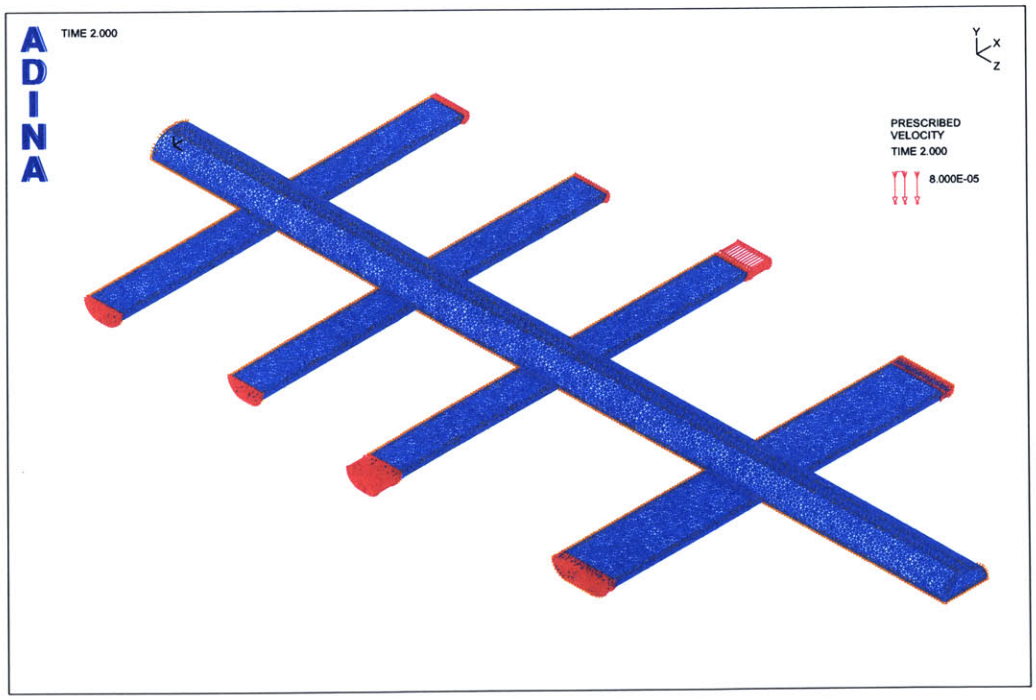

```
* Command file created from session file information stored within AUI database
*
*--- Database created 13 April 2007, 00:00:00 ---*
*--- by ADINA: AUI version 8.4.1 ---*
*
DATABASE NEW SAVE=NO PROMPT=NO
FEPROGRAM ADINA
CONTROL FILEVERSION=V84
*
FEPROGRAM PROGRAM=ADINA-F
*
FEPROGRAM PROGRAM=ADINA-F
*
LOADSOLID PARTFILE='C:\TAL\CorrectedFocusing\40X100.40X100.x_t' BODYNAME=1,
   XORIGIN=0.00000000000000 YORIGIN=0.00000000000000,
   ZORIGIN=0.00000000000000 AX=1.00000000000000 AY=0.00000000000000,
   AZ=0.00000000000000 BX=0.00000000000000 BY=1.00000000000000,
   BZ=0.00000000000000 PCOINCID=YES PCTOLERA=1.00000000000000E-06,
   MANIFOLD=NO FORMAT=TEXT OLD-UNIT=METER NEW-UNIT=METER SYSTEM=0,
   REPAIR=NO
*
MASTER ANALYSIS=STEADY-STATE MODEX=EXECUTE TSTART=0.00000000000000,
   IDOF=1 TURBULEN=NO HYDRO=YES STREAM=YES TRACTB=DEFAULT,
   IRINT=DEFAULT AUTOMATI=NO SOLVER=DEFAULT COMPRESS=NO FSINTERA=NO,
   NMASS=0 MASSCOUP=NO MAP-OUTP=NONE MAP-FORM=NO NONDIMEN=NO,
   MAXSOLME=0 MTOTM=2 RECL=3000 ALE=NO THERMAL-=NO,
   UPWINDIN=CONTROL-VOLUME MESHUPDA=CURRENT MESHADAP=NO,
   COUPLING=ITERATIVE POROUS-C=NO CELL-BCD=YES VOF=NO FCBI=YES,
   TURB-ITE=COUPLED EM-MODEL=NO ALE-CURV=YES ADAPTIVE=''
*
TOLERANCES GEOMETRIC COINCIDE=1.00000000000000E-07,
   EPSILON=1.00000000000000E-09 NCTOL-TY=RELATIVE-LOCAL
*
TIMESTEP NAME=DEFAULT
@CLEAR
4 0.500000000000000
@
*
TIMEFUNCTION NAME=1
@CLEAR
0.00000000000000 0.00000000000000
2.00000000000000 1.00000000000000
@
*
MATERIAL CONSTF NAME=1 XMU=0.000890000000000000 CP=0.00000000000000,
   XKCON=0.00000000000000 BETA=0.00000000000000 QB=0.00000000000000,
   RHO=1000.00000000000 TREF=0.00000000000000,
   GRAV-X=0.00000000000000 GRAV-Y=0.00000000000000,
   GRAV-Z=0.00000000000000 SIGMA=0.00000000000000,
   KAPPA=1.00000000000000E+20 CV=0.00000000000000 MDESCRIP='Water'
*
EGROUP THREEDFLUID NAME=1 MATERIAL=1 RSINT=3 TINT=3 RESULTS=STRESSES,
   DISSP=NO SOLID=NO UPWINDIN=DEFAULT OPTION=NONE FLOWTYPE=DEFAULT,
   VOF-MATE=1 DESCRIPT='Water'
*
MASTER ANALYSIS=STEADY-STATE MODEX=EXECUTE TSTART=0.00000000000000,
   IDOF=1 TURBULEN=NO HYDRO=YES STREAM=YES TRACTB=DEFAULT,
   IRINT=DEFAULT AUTOMATI=NO SOLVER=DEFAULT COMPRESS=NO FSINTERA=NO,
   NMASS=0 MASSCOUP=NO MAP-OUTP=NONE MAP-FORM=NO NONDIMEN=YES,
   MAXSOLME=0 MTOTM=2 RECL=3000 ALE=NO THERMAL-=NO,
   UPWINDIN=CONTROL-VOLUME MESHUPDA=CURRENT MESHADAP=NO,
   COUPLING=ITERATIVE POROUS-C=NO CELL-BCD=YES VOF=NO FCBI=YES,
   TURB-ITE=COUPLED EM-MODEL=NO ALE-CURV=YES ADAPTIVE=''
*
MASTER ANALYSIS=STEADY-STATE MODEX=EXECUTE TSTART=0.00000000000000,
   IDOF=1 TURBULEN=NO HYDRO=YES STREAM=YES TRACTB=DEFAULT,
   IRINT=DEFAULT AUTOMATI=NO SOLVER=DEFAULT COMPRESS=NO FSINTERA=NO,
   NMASS=0 MASSCOUP=NO MAP-OUTP=NONE MAP-FORM=NO NONDIMEN=YES,
   MAXSOLME=0 MTOTM=2 RECL=3000 ALE=NO THERMAL-=NO,
   UPWINDIN=CONTROL-VOLUME MESHUPDA=CURRENT MESHADAP=NO,
```

```
   COUPLING=ITERATIVE POROUS-C=NO CELL-BCD=YES VOF=NO FCBI=YES,
   TURB-ITE=COUPLED EM-MODEL=NO ALE-CURV=YES ADAPTIVE="
*
NONDIMENSION INPUT=YES OUTPUT=NO L=1.000000000000000E-06,
   XREF=0.00000000000000 YREF=0.00000000000000,
   ZREF=0.00000000000000 V=1.000000000000000 D=1.00000000000000,
   CP=1.00000000000000 T=1.00000000000000 TREF=0.00000000000000
*
MASTER ANALYSIS=STEADY-STATE MODEX=EXECUTE TSTART=0.00000000000000,
   IDOF=1 TURBULEN=NO HYDRO=YES STREAM=YES TRACTB=DEFAULT,
   IRINT=DEFAULT AUTOMATI=NO SOLVER=DEFAULT COMPRESS=NO FSINTERA=NO,
   NMASS=0 MASSCOUP=NO MAP-OUTP=NONE MAP-FORM=NO NONDIMEN=YES,
   MAXSOLME=0 MTOTM=2 RECL=3000 ALE=NO THERMAL-=NO,
   UPWINDIN=CONTROL-VOLUME MESHUPDA=CURRENT MESHADAP=NO,
   COUPLING=ITERATIVE POROUS-C=NO CELL-BCD=YES VOF=NO FCBI=YES,
   TURB-ITE=COUPLED EM-MODEL=NO ALE-CURV=YES ADAPTIVE="
*
SUBDIVIDE BODY NAME=1 MODE=LENGTH SIZE=1.50000000000000E-05
@CLEAR
1
@
*
SUBDIVIDE EDGE NAME=1 BODY=1 MODE=LENGTH SIZE=1.00000000000000E-05
@CLEAR
13
15
21
24
29
32
37
40
17
18
28
26
36
34
44
42
@
*
BODY-DISCREP NAME=1
*
BODY-DEFEATU NAME=1 SIZE=5.000000000000000E-06 DOMKEEP=0 DOMREMV=0,
   PREVIEW=NO OPTION=COARSEN ANGLE=60.0000000000000 SPREAD=YES
*
GBODY NODES=4 NCOINCID=BOUNDARIES NCTOLERA=1.000000000000000E-07,
   SUBSTRUC=0 GROUP=1 PREFSHAP=AUTOMATIC COLLAPSE=NO SIZE-FUN=0,
   DELETE-S=NO ANGLE-MI=5.00000000000000 MIDNODES=CURVED,
   METHOD=DELAUNAY PATTERN=0 MESHING=FREE-FORM DEGENERA=YES,
   BOUNDARY=DELAUNAY DEG-EDGE=0 GEO-ERRO=0.000000000000000,
   SAMPLING=20 MIN-SIZE=0.00000000000000 NLAYER=1 NLTABL=0,
   AUTO-GRA=NO SIMULATE=NO PYRAMIDS=NO DANGMAXB=80.0000000000000,
   DANGMAXC=60.0000000000000 DANGMAXD=80.0000000000000 HEXALAYE=NO,
   AUTO-REF=YES EVEN=SUM DENSITY=1.80000000000000
@CLEAR
1 0
@
*
BOUNDARY-CON WALL NAME=1 GTYPE=FACES SLIPC=0.00000000000000 MOVING=NO,
   BODY=1 VTYPE=CONVENTIONAL VT=0.00000000000000 NCURVT=0,
   DX=1.00000000000000 DY=0.00000000000000 DZ=0.00000000000000,
   X0=0.00000000000000 Y0=0.000000000000000 Z0=0.00000000000000,
   ALL-EXT=NO THERMAL=HEAT-FLUX TVALUE=0.00000000000000 NCURT=0
@CLEAR
1 0
2 0
3 0
4 0
```

```
5 0
6 0
7 0
8 0
10 0
11 0
12 0
13 0
14 0
15 0
16 0
17 0
18 0
19 0
20 0
21 0
22 0
23 0
24 0
25 0
26 0
27 0
28 0
29 0
30 0
@
*
LOAD VELOCITY NAME=1 VX=-.200e-4 VY=0.0 VZ=0.0
*
LOAD VELOCITY NAME=2 VX=.200e-4 VY=0.0 VZ=0.0
*
LOAD VELOCITY NAME=3 VX=-.100e-4 VY=0.0 VZ=0.0
*
LOAD VELOCITY NAME=4 VX=.100e-4 VY=0.0 VZ=0.0
*
LOAD VELOCITY NAME=5 VX=-.700e-4 VY=0.0 VZ=0.0
*
LOAD VELOCITY NAME=6 VX=.700e-4 VY=0.0 VZ=0.0
*
LOAD VELOCITY NAME=7 VX=.200e-4 VY=0.0 VZ=0.0
*
LOAD VELOCITY NAME=8 VX=-.200e-4 VY=0.0 VZ=0.0
*
APPLY-LOAD BODY=1
@CLEAR
1 'VELOCITY' 1 'FACE' 34 0 1 0.00000000000000 0 0.00000000000000,
   0.00000000000000 1
2 'VELOCITY' 2 'FACE' 33 0 1 0.00000000000000 0 0.00000000000000,
   0.00000000000000 1
3 'VELOCITY' 3 'FACE' 32 0 1 0.00000000000000 0 0.00000000000000,
   0.00000000000000 1
4 'VELOCITY' 4 'FACE' 31 0 1 0.00000000000000 0 0.00000000000000,
   0.00000000000000 1
5 'VELOCITY' 5 'FACE' 35 0 1 0.00000000000000 0 0.00000000000000,
   0.00000000000000 1
6 'VELOCITY' 6 'FACE' 36 0 1 0.00000000000000 0 0.00000000000000,
   0.00000000000000 1
7 'VELOCITY' 7 'FACE' 38 0 1 0.50000000000000 0.5 0.00000000000000,
   0.00000000000000 1
8 'VELOCITY' 8 'FACE' 37 0 1 0.50000000000000 0.5 0.00000000000000,
   0.00000000000000 1
@
```

Bibliography

[1] J.H. Aborn, S.A. El-Difrawy, M. Novotny, E.A. Gismondi, R. Lam, P. Matsudaira, B.K. Mckenna, T. O'Neil, .P Streechon, and D.J. Erhlich. A 768-lane microfabricated systemf for hight-throughput dna sequencing. *Lab Chip*, 2005.

[2] D.L. Chen, C.J. Gerdts, and R.F. Ismagilov. Using microfluidics to observe the effect of mixing on nucleation of protein crystals. *Journal of the American Chemical Society*, 127(27):9672–9673, 2005.

[3] M.W. Davidson and K.R. Spring. *Basic Concepts and Formulas in Microscopy - Depth of Field and Depth of Focus*. Nikon MicroscopyU.

[4] N.E. Dorsey. *Properties of Ordinary Water-Substance*. New York, 1940.

[5] Christopher J. Easley, James M. Karlinsey, Joan M. Bienvenue, Lindsay A. Legendre, Michael G. Roper, Sanford H. Feldman, Molly A. Hughes, Erik L. Hewlett, Tod J. Merkel, Jerome P. Ferrance, and James P. Landers. A fully integrated microfluidic genetic analysis system with sample-in-answer-out capability. *PNAS*, 103(51):19272–19277, 2006.

[6] Melles Griot. *The Practical Application of Light*. Barloworld Scientific, 2006.

[7] M.R. Holl, P. Galambos, F.K. Forster, J.P. Brody, M.A. Afromowitz, and P. Yager. Optimal design of a microfabricated diffusion-based extraction device. In *Proceedings of 1996 ASME Meeting ASME DSC59*, 1996.

[8] B. Huang, H. Wu, B. Devaki, A. Grossman, S. Granier, B. Kobilka, and R. Zare. Counting low-copy number proteins in a single cell. *Science*, 2007.

[9] A. Jahn, W.N. Vreeland, M. Gaitan, and L.E. Locascio. Controlled vesicle self-assembly in microfluidic channels with hydrodynamic focusing. *Journal of the American Chemical Society*, 126(9):2674–2675, 2004.

[10] K.F. Jensen, J. Han, D.J. Harrison, and J. Voldman, editors. *Proceeding of Micro Total Analysis Systems*, number 9 in International Conference on Miniaturized Systems for Chemistry and Life Sciences, Boston, October 2005.

[11] G.-B. Lee, C.-H. Lin, and S.-C. Chang. Micromachine-based multi-channel flow cytometers for cell/particle counting and sorting. *Journal of Micromechanics and Microengineering*, 15:447–454, March 2005.

[12] J.M.K. Ng, I. Gitlin, A.D. Stroock, and G.M. Whitesides. Components for integrated poly(dimethylsiloxane) microfluidic systems. *Electrophoresis*, 2002.

[13] Y.J. Pan, J.J. Lin, W.J. Luo, and R.J. Yang. Sample flow switching techniques on microfluidic chips. *Biosensors and Bioelectronics*, 2006.

[14] C. Simonnet and A. Groisman. Two-dimensional hydrodynamic focusing in a simple microfluidic device. *Applied Physics Letters*, 87(11):114104, 2005.

[15] T.M. Squires and S.R. Quake. Microfluidics: Fluid physics at the nanoliter scale. *Reviews of Modern Physics*, 77(3):977, 2005.

[16] T. Stiles, R. Fallon, T. Vestad, J. Oakey, D.W.M. Marr, J. Squier, and R. Jimenez. Hydrodynamic focusing for vacuum-pumped microfluidics. *Microfluidics and Nanofluidics*, 2005.

[17] A. D. Stroock, S. K. W. Dertinger, A. Ajdari, I. Mezic, H. A. Stone, and G. M. Whitesides. Chaotic mixer for microchannels. *Science*, 295(5555):647–651, 2002.

[18] T. Thorsen, R. W. Roberts, F. H. Arnold, and S. R. Quake. Dynamic pattern formation in a vesicle-generating microfluidic device. *Phys. Rev. Lett.*, 86(18):4163–4166, Apr 2001.

[19] M.M. Wang, E. Tu, D.E. Raymond, J.M. Yang, N. Hagen, B. Dees, E.M. Mercer, A.H. Forster, I. Kariv, P.J. Marchand, and W.F. Butler. Microfluidic sorting of mammalian cells by optical force switching. *Nature Biotechnology*, 2005.

[20] R. Yang, D.L. Feeback, and W. Wang. Microfabrication and test of a three-dimensional polymer hydro-focusing unit for flow cytometry applications. *Sensors and Actuators*, 2005.